TOPIC "Impact of radar penetration" (Sect 3.2)

Comment of the referee:

The section should concentrate on /emphasize a conclusion on the extensively described distribution of σ0. In the end, a mask with σ0 thresholds as a function of elevation, look angle incidence angle, date/time etc. would be precious. It would enable applicability of this new method for future studies. At the moment the procedure leaves the reader with the barrier 'done by expert knowledge' and no chance to use or reproduce the method. If changing that is out of scope, at least the numeric outcome of the method should be supported by more than one resulting number which up to now is limited to the final ε$_{pen}$ in the supplement.

So far, the end of 3.2.1 reads (p11ll7): 'The offsets are based on empirical observations of the relationship between σ0 and height offset performed on multiseasonal TDM Raw DEMs of NPI, showing a mean penetration bias of 4 m for an increase of σ0 by 10 dB from wet to dry snow (Abdel Jaber, 2016).

Please, add more precision to the cited paragraph: what exactly was applied then? A 4 m mean penetration depth assumed for all masked areas? Or if not, how is it calculated/modelled? Moreover, the description in p13ll15 stays vague, except for 6 m as a maximum.
Provide a conclusion about applied thresholds (σ0 etc.) in the text at the end of 3.2.2 similar to the cited one.
Provide numeric values for the assumed (mean?) penetration depth at each location in Fig. S5 referring to the manually outlined areas they are applied to.

Response:

We agree on this point raised by the referee. In order to make the publication increasingly independent of other publications we rephrased the last sentence and added a section on estimation of penetration offset on the critical regions to the Supplement (included in Sect. S5). We explain the relationship between σ0 and the penetration bias which was used to derive the penetration offsets for subareas covered by non-melting snow surfaces according to the increased backscatter coefficient. The percentage of NPI and SPI accumulation area included in the critical regions and the related elevation biases are specified in Table S6 for the SRTM and TDM DEM mosaics.

TOPIC "DEM Coregistration" (sect. 3.1.2) and following error contribution (Sect. 3.3.3)

Comment of the referee:

I summarize: Coregistration is done by manual APO updates through ITP processing with regard to ref. DEM (TDX 0.4 arcsec). Further efforts are claimed to not be necessary for TanDEM products. NASADEM was vertically adjusted, horizontal adjustment was checked to be needless. I suggest support the precision of this process, which is of key importance to geodetic method, with statistical values more adequate than the provided ones.

Therefore, I want to emphasize again: If you assess the error on the same CRs, where you corrected the offset, you get the residual error of the values you calibrated your model with. Not the error of the values you claim it to be valid for which is all the rest of each DEM. It for sure is possible to find some VRs (validation regions) with similar properties as the CRs. Show the spread of height diff to reference DEM there. Including slopes up to 20° in this validation process would solve two problems: 1) the dependence of the elevation difference to slope could be addressed. 2) the claim that horizontally no shifts remain, could be padded, since they appear more significantly with slope. Values would point to a positive /negative distribution center corresponding to the spread of aspects in the corresponding scene if residual hor. shifts remain.

revise the systematic error contribution of ε_{reg}:
Do not use error values on CRs. Statement above.
Do not apply IQR: The process does not cut outliers but reduces the systematic error component to its lower half. You responded: 'The IQR was chosen instead of standard deviation because the distribution is not Gaussian' → If DEMs are hor. and vert. coregistered, the residual height error should be normally distributed.

How is the absence of horizontal shifts checked? The detection is slope dependent (cf.Nuth and Kääb (2011)), thus cannot be efficiently performed on an area without slope as the CRs (avr. slope below 4)
Response: The horizontal shifts (in our case possibly acting in the ground range direction) were not checked analytically directly on our datasets, but relying on visual analysis of all available off-glacier terrain. Analytical checks using the method of Nuth and Kääb (2011) was done for the TDM-SRTM SEC datasets during the preparation of the thesis (Abdel Jaber et al., 2016) corroborating the validity of this calibration procedure. Because the same method was applied for this paper as for the thesis, the conclusions regarding this procedure can be adopted for this work.

→ Concerning the last two sentences, the thesis reads:
'The horizontal coregistration with respect to the SRTM appears to be achieved as well: the difference images do not display a hillshade effect (see Figure 7.9) and the method of Nuth & Kääb (2011) confirmed the validity of the correction. The quality of

the coregistration was furthermore confirmed by comparing on stable terrain (ice-free) the corrected TanDEM-X Raw DEMs and the SRTM C-band DEM to several ICESat GLAS altimetry tracks acquired between 2003 and 2009. Nevertheless a certain amount of residual horizontal misregistration can be expected, given the uncertainty linked to the height offset estimation. Its contribution will be accounted in the mass balance error budget'(Abdel Jaber 2016, p 91)
There is no statistical / numerical evidence referenced, but a Figure to check the absence of aspect dependent slope offsets visually. It is due to such a response, that I must insist in you taking the suggestion seriously that I repeat here: Put more effort to divide the thesis and the paper, to make latter a scientific stand-alone document. For this specific case: Even if the method is applicable, please show this, by validating your data independently as suggested in >Comments on 3.1.2 Coregistration of DEMs and following error contribution in 3.3.3<.

Response:

The error estimation intends to model the error associated, in this case, with the coregistration procedure. It is not intended as a validation. The number of calibration regions is limited for each Raw DEM (less than 20, less than 10 for some Raw DEMs). The IQR is calculated on their μ_r (mean of Δh with respect to the TDM global DEM on the CR pixels) as a measure of spread, the rationale being that the larger the spread within a Raw DEM, the less certain is the obtained height offset and the corresponding APO value used for coregistration of that Raw DEM. The distribution of these limited number of μ_r is not Gaussian and the IQR was chosen over the standard deviation as it leads to a more conservative error estimate for almost all Raw DEMs.

Concerning the issue of horizontal shifts we would like to emphasize that the slope distribution on the icefields is significantly skewed towards low slopes. Figure 1 shows the slope distribution and cumulative slope distribution of NPI and SPI. It can be appreciated that 80% of the icefield surface has a slope lower than 15° on NPI and lower than 23° on SPI.

The small residual horizontal shifts in ground range direction which might affect each Raw DEM have consequently a negligible vertical offset effect on most of the icefield surface.

Nevertheless in order to fully tackle the concerns raised by the referee, we include for each SEC dataset the maps of the elevation difference on stable terrain (except some small glaciers not belonging to SPI and NPI which were not masked out). These are show in Fig. 2 for the datasets of NPI 2000-2012 (a), NPI 2012-2015 (b) and in Fig. 3 for the datasets of SPI 2000-2012 (a), SPI 2012-2015 (b). The images further highlight in magenta the location and coverage on the calibration regions (CRs). These images were requested by both referees, we cannot at the moment include them in the Supplement since this has already reached the maximum allowed size (50 MB). We will gladly include them if this size limitation can be technically overcome. The TDM vs. TDM differences display very good alignment according to Fig. 2(b) and Fig. 3(b). In the NASADEM vs. TDM some vertical biases (of varying amplitude and sign) as well as some horizontal shift of varying direction are visible in different regions of the off-glacier terrain. These are mostly due to long-wavelength biases still affecting the NASADEM caused by the mosaicking

procedure and by oscillations of the mast on the Space shuttle, nevertheless we noticed a significant improvement compared to the previous SRTM v3 (see Manuscript Sect. 2.2 and Supplement Section S2). Furthermore on the steep terrain surrounding the icefields the elevation difference caused by the different resolution of the TanDEM-X and of the NASADEM DEM is noticeable. This bias is however are not critical on the icefield, characterized mostly by low slope and curvature.

We computed some statistical values, as requested by the referee. In particular we extracted mean and standard deviation of the elevation difference on off-glacier samples with slope below 20° for each SEC dataset.

Table 1: off-glacier, off-water mean and standard deviation for SEC samples with slope below 20° for all SEC datasets.

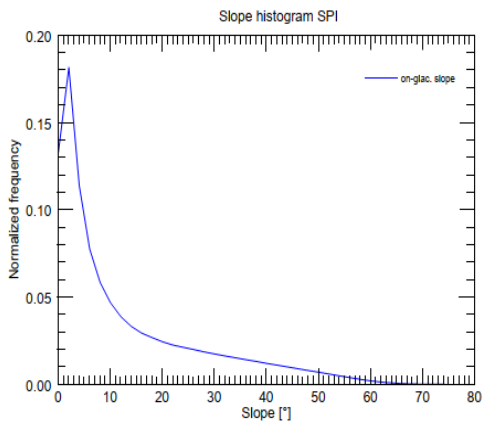| Dataset	**NPI 2000 – 2012**	**NPI 2012 – 2015**	**SPI 2000 – 2012**	**SPI 2012 – 2015**
Samples	13 969 156	11 486 375	37 455 616	22 332 512
Mean Δh [m]	0.060	0.210	0.094	0.104
Std. Dev. Δh [m]	6.316	3.977	6.741	4.328
Mean slope [°]	9.191	8.942	11.465	11.356
Std. Dev. slope [°]	6.011	5.977	5.52988	5.531
Mean NASADEM [m]	367.445	320.093	506.158	449.338
Std. Dev. NASADEM [m]	395.951	381.113	400.440	360.240

It must be noted that the off-glacier areas, especially those featuring a rough topography have not been subject to a thorough outlier masking. Small areas of phase unwrapping error, layover and shadow are still present and might affect the statistics. These are hence to be considered a worst-case scenario compared to the SEC on-glacier.
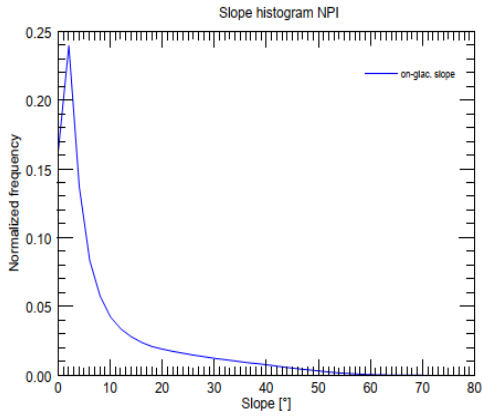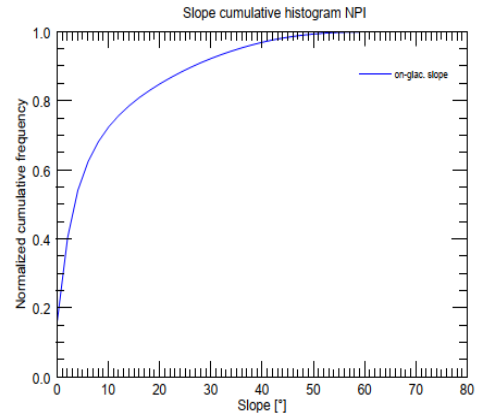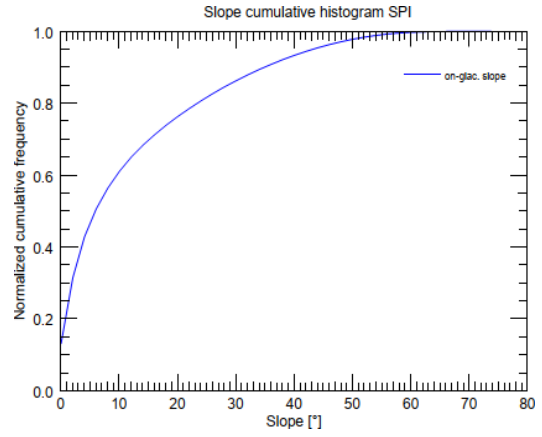
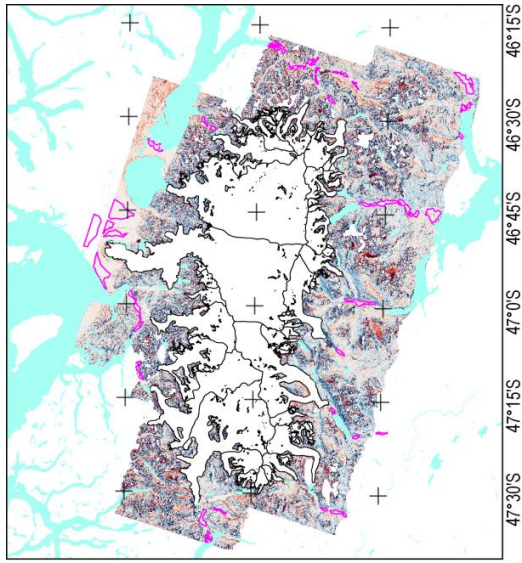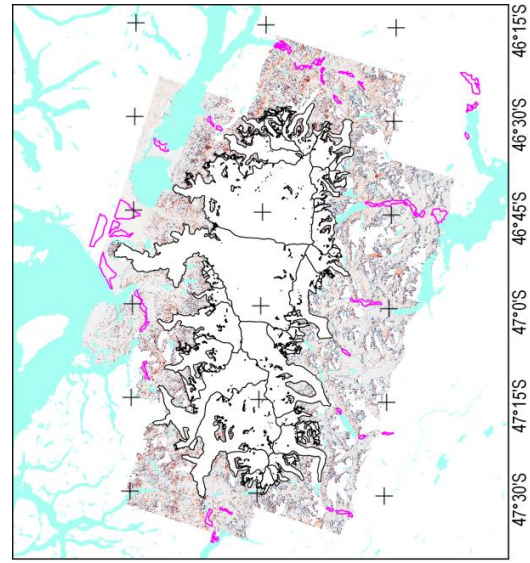Figure 1: Slope distribution of NPI (a) and SPI (c). Cumulative slope distribution of NPI (b) and SPI (d).

Figure 2: off-glacier elevation difference for NPI 2000-2012 (a) and NPI 2012-2015 (b). The color scale is the same as in Fig.3.
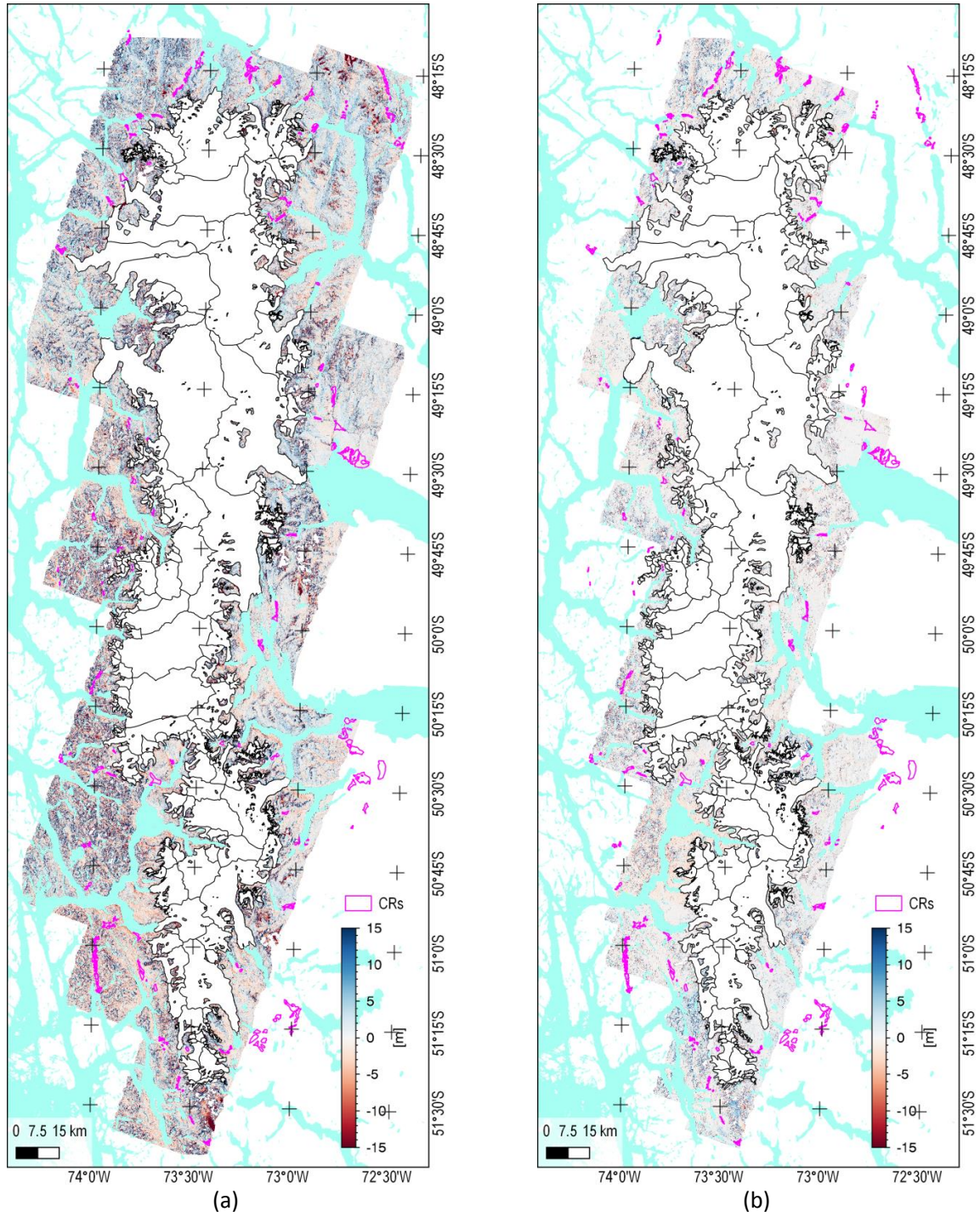
Figure 3: off-glacier elevation difference for the SEC datasets SPI 2000-2012 (a) and SPI 2012-2015 (b).

TOPIC "Seasonal correction" (Sect. 3.1.3)

Comment of the referee:

What kind of filtering was applied? It would be interesting to see the original dataset and a Δh map outside the icefields.
Response: Since the Summer 2011/2012 daily SECR is used only for the seasonal correction, we applied the following procedure for eliminating outliers: (i) conservative masking on glaciated terrain of regions with high backscattering and peaks in the daily SECR values followed by (ii) 2-step filtering with sliding 15window: (a) median filters with kernel size 9 and (b) smoothing with kernel size 9. The raster posting is 0.4 arcsec. This way the localized seasonal changes or outliers were eliminated and thus the SECR map can be used for the purpose of compensating the temporal gap in 2015/2016.
→ A shortened description would complement the caption of Fig8. Please consider reproducibility, not only answering to me.

Response:

Our response was not intended exclusively for the referee but rather to the general public reading the author's response available online. The caption was changed as suggested by the referee.

TOPIC "Filtering of outliers" (Sect. 3.1.4)

Comment of the referee:

Can you please add more information to increase reproducibility when data gets available: what threshold on SEC values? What morphological operators?
Response: We did not include these details because we do not think that this is an interesting point and would inflate an already very long paper. For each of the 4 SECR maps we produced a raster starting from the flag mask (FLM) layer that resulted from the processing with ITP which provides roughly the regions affected by layover and shadow. Thresholds h/t < -10 m/a and > +6 m/a were applied. A morphological operator of closing followed by a 5 x 5 median filter was applied on the mask raster in order to "clean" the mask, avoiding noise due to thresholding.
→ Eliminating the phrase from the manuscript does not support transparency.
Please integrate answer in manuscript /supplement. Especially the asymmetrical thresholding is interesting. Please provide reasoning for that. A symmetrical cut-off for outlier elimination would be methodically sounder. Executed like provided, statistically appearing (therefore normally distributed) residual noise error resulting in higher/lower rates gets dragged to more negative rates

Response:

We added the requested reasoning to the Supplement (in Sect. S3) and referenced it in the manuscript. The asymmetrical thresholds wrongly given in the previous version of the response have been corrected.

TOPIC "Seasonal correction systematic error" (Sect. 3.3.3)

Comment of the referee:

According to this paragraph: for interpolated seasonal correction, the last epsilon term should dominate the quadrature sum and thus the total SECR error, if I understand correctly. What does 'increase by a factor of three' mean in this context? Times 3 (*3) ? I compared SECR uncertainty value for extrapolated glaciers (e.g. Jorge Montt, Bernardo, Tempano) in Tab. 3 with values for not extrapolated glaciers. First ones are not near triple of latter. And they should even be higher than triple, following this paragraph: scaling by year (divided by 0.27. for 99 days for example) is performed as well as a *1.5 increase for the timespan difference. Please explain where I've gone wrong and/or revise the explanations in this paragraph.

Response: Thanks for pointing this out. It seems there is some misunderstanding regarding the seasonal correction and its impact for the retrieval of SECR. The term seasonal correction refers to the difference between mean annual SECR over epochs spanning 12 years (2000 to 2012) and 4 years (2012 to 2016) without accounting for seasonal differences in SEC of the missing days vs. the mean annual SECR taking seasonal differences into account. For the extrapolated glaciers 53 to 103 summer days are missing in order to cover the full 4 year period (1461 days). This means that the missing days to be substituted correspond to 3.6 % to 7.0 % of the 4 year period for which the mean SECR is computed (and not 27 % which would refer to a single year). The impact of missing days to be substituted for the 12 year period I still much smaller. This is now made clear in the revised section 3.1.3 and in Supplement S4.

→ Thank you for correcting my wrong assumption. It really helped understanding the seasonal correction – as well as the revision of the respective section. Yet, it also emphasized the relatively small impact of the correction to the results. After reviewing the paragraph of the related error estimation again, I now understood correctly what has been done and am sorry about misconceptions. Still I suggest a little step to improve the manuscript.

The paragraph p13ll26 reads:
To compute the systematic error linked to the seasonal correction (Sect. 3.1.3), the previous three systematic error components (ε reg , ε pen and ε add) were estimated separately for the summer 2011/2012 SECR. Here ε add was increased by a factor of 1.5 to account for the different temporal coverage. All three components were summed in quadrature and conservatively further increased by a factor of 3.0 on extrapolated regions (north of SPI and NPI). A pixelwise scaling by the number of corrected days and by the appropriate Δt in years was applied, leading to a fourth systematic error
The calculation in the cited paragraph is:
(1) $\varepsilon seas (x, y) = sqrt(\varepsilon reg^2 + \varepsilon pen^2 + (1.5*\varepsilon add)^2) *days)/\Delta t$
(2) $\varepsilon seas (x, y) = sqrt(\varepsilon reg^2 + \varepsilon pen^2 + (1.5*\varepsilon add)^2)*3 *days)/\Delta t$ (for extrapolated regions)
I assume. since you involved this error contribution from a seasonal yearly change rate scaled to the

dh error, in this case the Δt=365days. This practice is fine, and I misunderstood it in the first place. That might be, due to the fact, that the phrasing in the last cited sentence indicates, that here a division by entire epoch would appear (Δt=4*356 d or 12*365 d respectively). Latter would be questionable, not representing what has been done, since you subsequently quadrature sum the epsilon components as

(3) $\varepsilon = sqrt(\varepsilon reg^2 + \varepsilon pen^2 + \varepsilon add^2 + \varepsilon seas^2)/\Delta t$

where the division by entire epoch appears as Δt to give an appropriate error budget for the SECR. → Please correct 'and by the appropriate Δt in years' to a phrasing that clarifies Δt to be 365d in this case.

Response:

The applied calculation is the following:

$\varepsilon seas''' (x, y)$ **[m]** = sqrt($\varepsilon reg^2 + \varepsilon pen^2 + (1.5*\varepsilon add)^2$)

in order to have the error on the elevation change rate we divide this by Δt_summer [d], the number of days separating master and slave of the summer SECR (either 99 or 33 days)

$\varepsilon seas'' (x, y)$ **[m/d]** = (sqrt($\varepsilon reg^2 + \varepsilon pen^2 + (1.5*\varepsilon add)^2$)) / Δt_summer [d]

Now for each pixel we multiply this error on the rate by the number of corrected days Δt_corr [d] for each multiyear dataset, and where extrapolation was performed also multiply it by a factor of 3.0.

$\varepsilon seas' (x, y)$ **[m]** = (sqrt($\varepsilon reg^2 + \varepsilon pen^2 + (1.5*\varepsilon add)^2$)) / Δt_summer [d] * Δt_corr [d]

$\varepsilon seas' (x, y)$ **[m]** = (sqrt($\varepsilon reg^2 + \varepsilon pen^2 + (1.5*\varepsilon add)^2$)) / Δt_summer [d] * Δt_corr [d] * 3.0

(for extrapolated regions)

Finally we obtain an error on the yearly rate, like with the other components dividing by the Δt [y].

We slightly modified the text in order to make the applied procedure even clearer.

Heterogeneous spatial and temporal pattern of surface elevation change and mass balance of the Patagonian icefields between 2000 and 2016

Wael Abdel Jaber[1], Helmut Rott[2,3], Dana Floricioiu[1], Jan Wuite[2], and Nuno Miranda[4]

[1]Remote Sensing Technology Institute (IMF), German Aerospace Center (DLR), Oberpfaffenhofen, Germany
[2]ENVEO IT GmbH, Innsbruck, Austria
[3]Institute of Atmospheric and Cryospheric Sciences, University of Innsbruck, Innsbruck, Austria
[4]European Space Agency (ESA) - ESRIN, Frascati, Italy

Correspondence to: Wael Abdel Jaber (wael.abdeljaber@dlr.de)

Abstract. The Northern and Southern Patagonian icefields (NPI and SPI) have been subject to accelerated retreat during the last decades with considerable variability in magnitude and timing among individual glaciers. We derive spatially detailed maps of surface elevation change (SEC) of NPI and SPI from bistatic SAR interferometry data of SRTM and TanDEM-X for two epochs, 2000–2012 and 2012–2016 and provide data on changes in surface elevation and ice volume for the individual glaciers and the icefields at large. We apply advanced TanDEM-X processing techniques allowing to cover 90 % and 95 % of the area of NPI and 97 % and 98 % of SPI for the two epochs, respectively. Particular attention is paid to precisely coregistering the DEMs, accounting for possible effects of radar signal penetration through backscatter analysis, and correcting for seasonality biases in case of deviations in repeat DEM coverage from full annual time spans. The results show a different temporal trend between the two icefields and reveal a heterogeneous spatial pattern of SEC and mass balance caused by different sensitivities in respect to direct climatic forcing and ice flow dynamics of individual glaciers. The estimated volume change rates for NPI are -4.26 ± 0.20 km^3 a^{-1} for epoch 1 and -5.60 ± 0.74 km^3 a^{-1} for epoch 2, while for SPI these are -14.87 ± 0.52 km^3 a^{-1} for epoch 1 and -11.86 ± 1.99 km^3 a^{-1} for epoch 2. This corresponds for both icefields to an eustatic sea level rise of 0.048 ± 0.002 mm a^{-1} for epoch 1 and 0.043 ± 0.005 mm a^{-1} for epoch 2. On SPI the spatial pattern of surface elevation change is more complex than on NPI and the temporal trend is less uniform. On terminus sections of the main calving glaciers of SPI temporal variations of flow velocities are a main factor for differences in SEC between the two epochs. Striking differences are observed even on adjoining glaciers, such as Upsala Glacier with decreasing mass losses associated with slowdown of flow velocity, contrasting with acceleration and increase of mass losses on Viedma Glacier.

1 Introduction

The Northern and Southern Patagonian icefields (NPI and SPI) are the largest contiguous temperate ice bodies in mid-latitudes of the southern hemisphere. They stretch from 46.5° S to 47.5° S and 48.3° S to 51.6° S, respectively, along the main ridge of the southern Andes and cover areas of about 4000 km^2 and 13000 km^2 (Davies and Glasser, 2012). The perturbation of the strong and consistent westerly flow caused by the Andes leads to one of the strongest precipitation gradients on earth (Garreaud

et al., 2013). Because the icefields are located on the only significant land mass between 45° S and Antarctica, they offer unique possibilities for studying the impact of changes in southern-hemisphere westerly flow on glacier evolution and for inferring Holocene climate history from glacial evidence (Rasmussen et al., 2007; Lopez et al., 2010; Glasser et al., 2011; Davies and Glasser, 2012; Garreaud et al., 2013).

Precise, spatially detailed data on changes of glacier area and volume and on the mass balance are essential for establishing reliable relations between climate signals and glacier records in order to reconstruct the past climate and to develop accurate predictive tools of glacier response to climate change (Fernández and Mark, 2016; Marzeion et al., 2017). The dynamic adjustment of a glacier to changing external forcing does not happen instantaneously. In particular for calving glaciers the dynamic behaviour and mass balance may be largely decoupled from direct climate forcing (Benn et al., 2007; Åström et al., 2014). The main outlet glaciers of the Patagonian icefields are tidewater or freshwater calving glaciers, showing heterogeneous patterns of changes in frontal position and hypsometry (Warren and Aniya, 1999). This stresses the need for spatially detailed geodetic repeat observations covering different epochs in order to resolve the complex pattern of glacial responses. High resolution topographic satellite data from SAR interferometry, as employed for the work reported in this paper, provide an excellent basis for handling these issues.

There has been a general retreat of SPI and NPI glaciers since the Little Ice Age (Davies and Glasser, 2012), however with considerable variability in magnitude and timing for individual glaciers. Only few glaciers advanced intermittently during recent decades. The most striking case is the Pio XI Glacier showing a large cumulative frontal advance since 1945, including recently a general advancing period of its southern and northern branches starting in 2000 and 2005, respectively (Wilson et al., 2016).

Geodetic mass balance estimates of NPI and SPI have been derived from various sources. The first remote sensing based estimates of NPI and SPI volume change and mass balance were reported by Rignot et al. (2003), comparing Shuttle Radar Topography Mission (SRTM) elevation data of February 2000 with topographic maps of 1968/1975 to estimate the volume change of the largest 63 glaciers. Elevation changes measured at low elevations were fitted to a polynomial as a function of elevation in order to extrapolate the results to higher elevations where the topographic maps have large gaps. A similar analysis was performed for 20 glaciers of SPI, where 1995 cartography is available, and scaled to infer the volume loss of the entire icefield.

The SRTM DEM was used in several studies as baseline for deriving volume change of the icefields during periods spanning the subsequent 10 to 15 years. Willis et al. (2012a, b) analyzed the ice volume change of NPI between 2000 and 2011 and of SPI between 2000 and 2012 by comparing the SRTM DEM with time series composed of 55 DEMs of NPI and 156 DEMs of SPI which were derived from data of the Advanced Spaceborne Thermal Emission and Reflection Radiometer (ASTER) operating on the Terra satellite. The authors used all suitable ASTER scenes and applied a weighted linear-regression to the time-series of elevations on a pixel-by-pixel basis in order to obtain the elevation change for the full time spans. Willis et al. (2012b) assumed a 2 m radar signal penetration bias for SRTM without taking into account the melting state of the surface. Introducing the same penetration bias, Willis et al. (2012b) revised also their previous volume loss estimate of NPI. This underlines the importance of correct treatment of radar signal penetration in case of interferometric DEMs. Dussaillant et al. (2018) determined the NPI

volume change for 2000 to 2012 with two methods, on one hand by differencing the SRTM DEM and a SPOT-5 DEM from March 2012, on the other hand by fitting pixel-based linear elevation trends over 118 DEMs calculated from ASTER stereo images acquired between 2000 and 2012. Icefield-wide rates of volume change by both methods agree very well.

Foresta et al. (2018) exploited swath processed CryoSat-2 interferometric data to produce maps of surface elevation change over the Patagonian icefields and estimated the mass balance for six years between April 2011 and March 2017. The maps cover 46 % of the total area of NPI, and 50 % of SPI with large gaps on the termini of most glaciers. Relations between CryoSat-2 elevation change and surface elevation in the SRTM DEM were used to fill the gaps in the surface elevation change (SEC) maps.

The TanDEM-X (TerraSAR-X add-on for Digital Elevation Measurements) mission (shortly TDM) (Krieger et al., 2007), composed of the two formation-flying radar satellites TerraSAR-X and TanDEM-X, is operational since December 2010. The mission opened up excellent new capabilities for high resolution topographic mapping of the global land surfaces including glaciers and ice sheets. Abdel Jaber (2016) generated DEMs based on comprehensive TanDEM-X data sets, over NPI mostly acquired in austral summer 2014 and over SPI between March 2011 and March 2012. DEM differencing versus the SRTM DEM yielded volume loss rates over NPI for the period 2000 to 2014 and over SPI for the period 2000 to 2011/2012. Abdel Jaber (2016) also presented detailed information on the methods used for DEM generation and calibration, on error assessment and on the analysis of radar backscatter signatures of SRTM and TDM drawing conclusions on radar signal penetration. For Jorge Montt Glacier, featuring the highest thinning rate on the icefield, the geodetic mass balance for 2011 to 2014 was also derived from TDM DEMs. Malz et al. (2018) performed DEM differencing of TDM DEMs of December 2015 versus the SRTM DEM over SPI. For the southern part of the SPI they further differentiated the SRTM elevation versus TDM DEMs from January–March 2012, autumn 2014 and winter 2016 and computed the TDM-based SEC for the epoch January–March 2012 to December 2015. Seasonal variations of surface elevation and of radar signal penetration were not taken into account for retrieving SEC rates.

The studies cited above use different data sets and methodological approaches and cover, at least to some extent, different epochs. This impairs the comparison of results, the evaluation of temporal trends and the analysis of commonalities and differences between the two icefields. In order to tackle these issues, we derive volume change of NPI and SPI exclusively from bistatic SAR interferometry (InSAR) data (SRTM and TDM) for two multi-annual periods, spanning from 2000 to 2012 and from 2012 to 2016. Furthermore, for the main retreating glaciers of SPI an estimate of subaqueous ice loss is provided for the period 2000–2011/2012. The generation of surface topography products and the analysis of elevation change build upon methods developed by Abdel Jaber (2016) with various upgrades regarding TDM data selection and processing methods. The results presented here are completely novel, unless clearly stated. Particular attention is paid to the acquisition dates of the different DEMs, applying corrections for deviations of repeat DEM coverage from full annual time spans in order to avoid seasonality biases when deriving annual SEC rates. Significant effort is dedicated to the assessment of the wetness of the snow and firn surface through a careful analysis of the backscatter of SRTM and TDM data, and to modelling and quantifying different sources of uncertainty.

The paper presents the first spatially detailed analysis of surface elevation change and the derived total net mass balance over the Patagonian icefields for two different epochs based on the same observation technique, including a catalogue of volume change for the epoch 2000 to 2012 and 2012 to 2016 for all glaciers > 2 km² of NPI and > 9 km² of SPI. The results indicate a different temporal trend between the two icefields and reveal the complex spatial pattern of SEC and mass balance as result of intricate interdependencies between direct climatic forcing and effects of ice flow dynamics.

2 Data

For the generation of surface elevation change rate (SECR) maps we rely exclusively on pairs of multitemporal bistatic InSAR DEMs. This technique provides wide-coverage surface elevation, overcoming issues affecting optical DEMs, such as lack of contrast on smooth snow or the presence of clouds, as well as the limited spatial coverage and resolution of altimeters. In this study we exploit data from TanDEM-X and SRTM, the sole earth observation systems equipped with single-pass radar interferometers.

2.1 TanDEM-X

The primary objective of the TanDEM-X mission is the generation of a global, consistent DEM with high resolution and accuracy (Krieger et al., 2007). The main payload of the twin satellites is a SAR instrument operating at X-band (9.65 GHz), capable of a swath width of 30 km in the operational Stripmap single-pol (HH) mode. The global DEM product (DLR-EOC, 2018), whose performances are analyzed in Rizzoli et al. (2017) and Wessel et al. (2018), is the result of the combination of four years of bistatic data acquisitions with different baselines and geometries. This product is hence not suitable for the derivation of surface elevation changes, nevertheless we exploited the 0.4 arcsec (~ 12 m) release as a reference DEM of the region for various processing aspects (Sect. 3), after proper editing of unreliable samples.

In this study we processed single, selected TDM bistatic raw datatakes into so-called Raw DEMs (Rossi et al., 2012; DLR-CAF, 2010) using ITP, the operational TanDEM-X processor (Breit et al., 2012; Fritz et al., 2011), in order to generate two elevation maps completely covering the icefields in the years 2012 and 2015. The TDM data selection for each coverage was based on various criteria like the reduction of temporal span and of the number of datatakes, warm seasons to minimize SAR signal penetration, small height of ambiguity (HoA) to reduce interferometric noise and similar imaging geometry. Ideally data acquisitions should be at the end of the ablation season when the surface is at its lowest, but most importantly the two coverages should be acquired at the same time of year in order to minimize seasonal changes, which can be significant on the Patagonian icefields. Since data availability restricted fulfilling the last criterium, the residual temporal gap had to be compensated.

The TDM acquisitions used to generate the two elevation maps are summarized in Tables S1 and S2 in the Supplement for NPI and SPI, respectively. The footprints of the individual Raw DEMs are shown in Fig. S1. The first elevation map is composed of descending acquisitions from austral summer 2012. An exception are the western termini of NPI where, due to data unavailability we had to rely on an acquisition from May 2011. The second coverage is achieved with descending acquisitions from December 2015 (beginning of austral summer). On part of SPI we additionally processed three acquisitions

from December 2011 acquired with the same geometry of the 2012 datatakes in order to measure seasonal elevation changes during summer. Three TDM datatakes from December 2015 (scenes 6 and 7 on NPI and 13 on SPI) feature a steep look angle ($< 27°$) leading to increased layover.

For each Raw DEM the ITP provides additional geocoded rasters (Rossi et al., 2010; DLR-CAF, 2010) which were used in different phases of this study: height error map (HEM), uncalibrated SAR amplitude, backscattering coefficient, interferometric coherence and flag mask indicating critical areas.

2.2 SRTM

The SRTM (Farr et al., 2007; Rabus et al., 2003) was launched 11 February 2000 and produced in 9 days of acquisition a near-global DEM (60° N–56° S) with 1 arcsec (~ 30 m) posting. The main payload was a bistatic C-band (5.36 GHz) SAR capable of a 225 km swath achieved applying the ScanSAR technique to four sub-swaths featuring different polarization (HH, VV, VV, HH) and look angles between 30° to 56°. The large number of interwoven acquisitions at higher latitudes contributed to both absolute and relative accuracy as well as to reducing voids: the 9 ascending and 9 descending datatakes covering the Patagonian icefields (Seal and Rogez, 2000) are listed in Table S3. The performance of SRTM was assessed among others by Rodriguez et al. (2005); Brown et al. (2005); Carabajal and Harding (2006); Wendleder et al. (2016). The main issue is the presence of long-wavelength height errors with magnitude up to ~ 20 m globally and spatial variation scales of hundreds to thousands of kilometres, mainly caused by residual roll errors due to the attitude adjustment manoeuvres of the Shuttle and by the applied absolute calibration of the sub-swaths.

The NASADEM (Crippen et al., 2016) is a new version of SRTM DEM, consisting of a complete reprocessing of the raw data, with improved phase unwrapping (significantly reducing voids) and an ICESat-based calibration, tackling issues such as limited absolute vertical accuracy and long-wavelength height errors. In this study we used a provisional version of NASADEM (NASA JPL, 2018) as the elevation map of year 2000 for both icefields. The choice was done after comparing on a vast region surrounding the Patagonian icefields the NASADEM and the SRTM ver. 3 (SRTMGL1) (NASA JPL, 2013) to the TDM global DEM rescaled to 1 arcsec. The SRTMGL1 data set, besides suffering from a vertical offset of ~ 1 m against the reference (statistics are given in Table S4), displays a stronger presence of long-wavelength elevation and geo-location biases (Δh images are shown in Fig. S2) and a higher RMS when compared to the NASADEM. On the icefields the differences between the two SRTM data sets are larger on NPI and in the very south of SPI.

We furthermore retrieved the SRTM radar brightness images (SRTMIMGR) (NASA JPL, 2014) for the sub-swaths covering the icefields (Table S3) with the purpose of assessing the melting state of the glacier surface. We also used the SRTM Water Body Data (SWBD) (Farr et al., 2007) for statistical and visualization purposes.

2.3 Glacier outlines

We relied on the Randolph Glacier Inventory (RGI) version 6 (RGI Consortium, 2017; Pfeffer et al., 2014), which contains improved basin divides of NPI by Rivera et al. (2007). We manually updated the RGI outlines at the glacier termini (including

5

internal rocks) using the SAR amplitude, the DEM and optical images in order to reflect the exact extent of the glaciers at the time of acquisition of each elevation map (2000, 2012, 2015).

3   Method and error estimation

3.1   Methods for SEC and mass balance

3.1.1   Raw DEM processing

The use of ITP to process the single Raw DEMs allows a great degree of flexibility with respect to processing parameters and algorithms. The beginning and end times of each scene were adapted (up to $\sim 30\,\text{s}$ total length) in order to minimize the number of scenes and to include the widest possible ice-free terrain suitable for DEM coregistration (Sect. 3.1.2). The ruggedness of the topography of the study region with its steep mountains and intricate water bodies poses a significant difficulty for the ITP operational algorithms of phase unwrapping (Lachaise, 2015) and absolute height determination (Rossi et al., 2012). We hence relied on an alternative algorithm of ITP (Lachaise and Fritz, 2016) which tackles both issues by exploiting an external reference DEM (Sect. 2.1).

The absolute phase simulated from the reference DEM is subtracted from the interferometric phase of the data. The fringe frequency of the differential phase is significantly lower and its unwrapping is unproblematic as long as elevation differences versus the reference DEM are not too large (maximum half of the HoA). The absolute phase of the data is then reconstructed by summing to the unwrapped differential phase the phase simulated from the reference DEM, this way removing any influence of the latter on the relative elevation in output. The output Raw DEM is finally obtained by geocoding in ITP the absolute phase of the data, implicitly determining an absolute phase offset (APO) value, on which the absolute height and the across-track position of the Raw DEM depends. ITP allows to manually update the APO value and perform a new geocoding, for instance to fine-tune the coregistration with a reference DEM, as described in Sect. 3.1.2.

3.1.2   DEM coregistration

The master and slave DEMs may be affected by vertical biases with respect to each other, these can be constant (offset), linear (tilt) or even varying with low frequency. They can furthermore be affected by horizontal shifts causing an additional slope- and aspect-dependent elevation bias in the SEC which couples with the vertical bias resulting in a systematic error with high potential impact on the volume change rate estimated over large areas. To obtain two consistent TDM elevation maps, coregistered to each other and -to the SRTM DEM we coregistered the single Raw DEMs and the SRTM DEMs of NPI and SPI to the reference DEM (Sect. 2.1).

An error in the APO of a TDM Raw DEM leads to a vertical height offset, an across-track horizontal shift and a tilt around the master flight trajectory (in order of impact, the latter being negligible in our Raw DEMs). These three effects are solved by fine-tuning the APO through an accurate estimation of the height offset versus the reference DEM and by repeating the geocoding with ITP. This method assures high precision by exploiting the geometrical parameters of the SAR acquisition and

allows avoiding critical aspects of the generic coregistration problem, accurately tackled by Nuth and Kääb (2011), such as estimation of horizontal shifts, interpolation, etc.

To estimate the height offset we manually selected a large number of calibration regions (CRs) over stable terrain around the icefields relying on the SAR amplitude, the TDM slope and optical imagery. Tall vegetation was avoided because of physical changes and varying scattering phase centre at different incidence angles and radar frequencies. The CRs were chosen to be as flat as possible in order to isolate the actual vertical height offset. Layover and shadow regions were avoided as well as water pixels, affected by low coherence. The footprints of the CRs are visualized in Fig. S1 and their features are summarized in Table S5.

From the elevation difference Δh between the reference DEM and the single Raw DEMs (or the SRTM DEMs of NPI and SPI) we computed on each CR with index r the mean μ_r, the standard deviation σ_r and the standard error of the mean:

$$\text{SE}_r = \frac{\sigma_r}{\sqrt{N_r}}, \tag{1}$$

where N_r indicates the number of spatially uncorrelated samples on CR r and was estimated through a semivariogram analysis as described in Sect. 3.3.2. A height offset estimate for each DEM was obtained through the weighted average

$$\delta h_{\text{off}} = \frac{\sum_r \frac{\mu_r}{\text{SE}_r^2}}{\sum_r \frac{1}{\text{SE}_r^2}}. \tag{2}$$

Values of δh_{off} ranged in magnitude between 0 m and 1.8 m for the TDM Raw DEMs and was used to fine-tune the APO. For the NASADEM the height offset δh_{off} was subtracted, this was equal to 0.3 m and 0.1 m in absolute value on NPI and SPI, respectively, and was. subtractResid-uafterl checking the horizontal coregshifts witrh spatioally varying wmagnitude might still be prespeent toin the TNASADEM, their eferfencet DEMon athe 0.4--arcsec inSECR of the picefields is neveroxtheless limityed, given that 80 % of the icefield surface has a slope lower than 15° and 23° on NPI and SPI, respectively.

Furthermore range and azimuth tilts caused by baseline errors (Hueso González et al., 2010) were verified and found to be negligible for all TanDEM-X Raw DEMs. Height consistency between overlapping Raw DEMs was also checked in order to ensure a seamless elevation map.

The coregistration procedure partly compensates the crustal uplift rates due to the glacial isostatic adjustment affecting the region, characterized by rates up to $40\,\text{mm}\,\text{a}^{-1}$ on the plateau of SPI and decreasing with distance as reported by Dietrich et al. (2010).

3.1.3 Seasonal correction

Seasonal variations of SECR should be taken into account for deriving annual rates of surface elevation change if the time span of the repeat DEMs does not exactly match yearly intervals. Commonly the mean daily SECR of the given time span is used for filling temporal gaps or for subtracting the contribution of excess days. This approach introduces a bias in annual SECR in case of seasonal variations. The magnitude of the bias depends on the percentage of missing (or excess) days and the amplitude of the seasonal cycle. The seasonal correction, as elaborated here, refers to the difference between mean annual SECR over

epochs of 4 years (2012 to 2016), respectively 12 years (2000 to 2012), taking seasonal differences in SECR for missing days into account versus mean annual SECR without accounting for such differences.

The temporal mismatch versus exactly 4 years and 12 years varies for the two epochs and for different sections of the ice fields. For 2012 to 2016 the impact of seasonal corrections is more important due to the shorter time span. For NPI the number of missing days corresponds to 3.6 % to 4.8 % of the 4-year time span, for the two main tracks acquired in February 2012. A small section of NPI (covering the lower termini of S. Rafael, S. Quintin and Benito glaciers) was instead acquired on 28 May 2011 (NPI scene No. 1; Table S1, Fig. S1a). For the main sections of SPI the percentage of missing days ranges from 3.6 % to 5.0 %, except for a small sub-area where it is 7 %. For SPI the 2000 to 2012 mismatch in percentage of the full period ranges from 0.1 % to 1.0 % of the 12-year period. Nevertheless, we applied seasonal corrections also to this data set. For the two tracks covering the main sections of NPI the gap corresponds to only 0.1% of the 12 years, given the limited surface covered by the third track, no correction was applied to this dataset.

Here we explain details on the seasonal correction for the epoch 2012–2016 because of their larger impact. Depending on the availability of additional TDM DEM data, the following procedures were applied for different sections of the icefields:

– Three additional TDM acquisitions of December 2011 (Table S2) cover the southern, central and north-western sections of SPI (59.4 % of SPI, Fig. **??**.). These data were used to compute daily SECR over summer 2011/2012 by DEM differencing vs. TDM data of March 2012 (99 days) covering the main part of SPI and vs. TDM data of 31 January 2012 (33 days) covering a sub-section in the south-east. The SECR maps of summer 2011/2012, scaled to the length of the missing period, were used for substituting the missing days in summer 2015/2016, a valid approach as the mean temperatures of the two summers agree within 0.1 °C. Air temperatures of the European Centre for Medium-Range Weather Forecasts Interim Re-Analysis (ERA-Interim) (Dee et al., 2011; Berrisford et al., 2011) show at the 850 hPa level for the grid point 47.25° S, 73.55° W (NPI) a mean summer temperature of 5.9 °C in 2011/2012 and 6.0 °C in 2015/2016, for point 50.25° S, 73.55° W (southern SPI) the values are 3.6 °C in 2011/2012 and 3.5 °C in 2015/2016.

– For SPI glaciers not covered by the summer 2011/2012 SEC map (except Pio XI and Jorge Montt glaciers) we used daily SECR in dependence of elevation derived from the 99-day SECR maps of summer 2011/2012 (blue curve in Fig. S3). For the section of Pio XI Glacier that is not covered by the summer SEC map we use the hypsometric SECR curve of low-loss glaciers (green curve in Fig. S3). On NPI, except on the termini covered by scene No. 1, we also used the hypsometric green curve of Fig. S3 since the majority of glaciers are not calving or the calving fluxes are a small component of total mass balance (Schaefer et al., 2013).

– For the three NPI termini covered by scene No. 1 and for Jorge Montt Glacier, which is not covered by the summer 2011/2012 SECR maps and subject to significant dynamic downwasting we separate the SEC component in the ablation areas related to surface melt from SEC due to dynamic downwasting. For this purpose estimates on the elevation dependence of the specific surface mass balance (SMB) during summer and the full year are needed. To our knowledge, up to now the only multi-year time series of ablation measurements on any glacier of SPI and NPI, including the separation of summer and annual periods, has been performed on Moreno Glacier (Stuefer et al., 2007). The applicability of the

8

Moreno mass balance elevation gradient has been checked by means of model output on SMB for NPI west coast glaciers (Schaefer et al., 2013) and mass balance data of Chico Glacier (Rivera, 2004), accounting for the west/east difference in temperature lapse rate across the icefield (Bravo et al., 2019). Further details are given in the Supplement, Sect. S4. The ratio between daily SMB-related SEC during summer vs. the rest of the year in dependence of elevation is used for estimating the increased SEC contribution due to surface melt during summer on the Jorge Montt terminus and for the reduced melt contribution during May to December for the three NPI termini. For the dynamic downwasting component we used the average SECR of the full period.

For the epoch 2000–2012 a seasonal correction was applied on SPI to the TDM elevations of 2012 to correct for the gap to the SRTM acquisition mid-date (17 February). The effect of the correction is small, being of main relevance for TDM scenes 6/7, acquired on 15 March 2012, covering $\sim$ 6000 km^2 with a temporal gap of 38 days. The two 99-days beams of the 2011/2012 summer SECR were used pixelwise where available. The hypsometric mean (blue curve in Fig. S3) was used elsewhere, with a reduction by 20 % to account for the late summer season (mid-February to mid-March). This scaling factor for late summer is based on a time series of daily air temperature measurements from 1995 to 2003 near the front of Perito Moreno Glacier and ablation data (Stuefer et al., 2007).

Finally the correction rasters were obtained by scaling pixelwise the daily correction rate by the temporal gaps in days (Fig. S4).

3.1.4 Derivation of SECR maps and estimation of mass balance

Two DEM mosaics were obtained for each icefield from the main TDM coverages by means of stacking, where the most reliable scene (evaluated through the height error, the look angle and the backscattering) was prioritized for overlapping regions. The WGS84 (EPSG:4326) projection with posting 0.4 arcsec was enforced through cubic convolution on a common geographic frame. Corresponding mosaics of the additional geocoded rasters computed by ITP were also obtained, as well as the SRTM DEM and its error layer. For each icefield two SECR rasters including seasonal correction were obtained differencing the DEM mosaics for the epochs 2000–2012 (12 years) and 2012–2016 (4 years), with the end of summer as reference start/end time of each epoch. To avoid biases of the mass balance we masked-out artefacts due to phase unwrapping, layover, shadow, etc. (Sect. S3 of the Supplement). The elevation of the water surface subject to frontal retreat, usually decorrelated, was manually edited in order to correctly capture the freeboard SEC.

By multiplying the average SECR with the corresponding glacier area over elevation intervals of 50 m the altitude-dependent volume change rate (VCR) was computed. The reference elevation used for the hypsometry is the 2012 TDM DEM (small voids are filled with the global DEM), which is common to the two investigation epochs. The mass balance was computed on the entire icefields as well as on single glaciers defined by the updated RGI glaciers outlines. The maximum extent of each glacier, either at the beginning or at the end of the observation period, was used to spatially capture all changes.

We used a glacier-wide density of 900 kg m^{-3} for the conversion of the VCR to mass change rate. This value is commonly used for geodetic mass balance measurements and provides traceability for comparisons with other studies (Cogley, 2009).

The main mass losses on the Patagonian icefields refer to ice areas, and for the accumulation areas assumptions on changes of the vertical profiles of snow/ice density would be speculative.

3.2 Impact of radar penetration

A critical issue affecting InSAR-based elevation data is the penetration of the radar signal in dry snow and firn. In this case the scattering phase centre is situated below the surface, causing an elevation bias in the DEM (Dall, 2007), ranging from decimetres to metres at C- and X-band. This represents an important source of local systematic error on the SEC and consequently on the resulting total net mass balance. The penetration depth depends on the microstructure and the dielectric properties of the snowpack, which are in turn strongly dependent on the liquid water content (LWC). Several models (Tiuri et al., 1984; Mätzler, 1987) show how at C- and X-band the penetration depth drops rapidly below 0.2 m already with a LWC of approximately 0.5 %^{vol}. We used the backscattering coefficient σ^0 as a proxy to assess the wetness status of the snow and firn (Ulaby et al., 2014; Mätzler, 1987). The C- and X-band radar return from the bare rough ice of the glacier termini is dominated by surface scattering so that penetration is not an issue here.

3.2.1 Assessment of TanDEM-X backscatter

The TanDEM-X sensor features an absolute and relative radiometric accuracy of 0.6 dB and 0.3 dB, respectively (DLR-CAF, 2013), allowing precise measurements of backscatter. For each Raw DEM we processed with the ITP the geocoded backscatter image including the annotated noise contribution. This typically varies between −29 dB and −17 dB along the range direction and can thus have a significant impact on σ^0 of weak scatterers such as smooth wet snow. The σ^0 mosaics corresponding to the 2012, 2015 and 2011 DEMs are shown in Fig. S5. No masking of artefacts was applied.

TDM austral summer datatakes were chosen in order to increase the likelihood of imaging wet snow and firn. The mid-range look angle (θ_l) ranges between 35° and 45°, except for scenes 6 and 7 of NPI and scene 13 of SPI which have steeper look angles (Tables S1 and S2). The satellite overpasses were at approximately 6:00 local time (UTC−4h), which is generally the coldest time of the day, although the plateaus of NPI and SPI usually feature limited daily variations of air temperature due to the dense clouds and strong precipitation occurring most of the year (Garreaud et al., 2013; Schaefer et al., 2013).

On the plateau of NPI (covered by scenes 2, 5, 6 in Table S1) $\sigma^0 < -18$ dB dominates in our dataset up to approximately 2300 m of altitude in 2012 and 2015 confirming high LWC on most of the surface. Above this altitude $\sigma^0 > -10$ dB can be found on limited areas (particularly in December 2015), implying the presence of dry snow. Some regions with $-15 < \sigma^0 < -11$ dB are found in scene 2 ($\theta_l = 38.4°$) at altitudes below 2000 m. Given the season and time of day, these can possibly be explained by the formation a refrozen crust layer on top of wet snow or firn, implying an offset of the scattering phase centre up to a few decimetres (Reber et al., 1987; Mätzler, 1987).

The backscattering of SPI is more heterogeneous compared to NPI. The 2015 coverage features $\sigma^0 \leq -19$ dB revealing wet snow on large parts of the plateau (particularly on the western margin). The σ^0 of the 2012 coverage is in average higher (especially on scene 4/5 acquired at the end of March). Over the main parts of the plateau σ^0 is still lower than −16 dB, an indication for wet snow, possibly covered locally by a thin frozen crust that would introduce only a small elevation bias. The

December 2011 coverage displays values of $\sigma^0 < -18$ dB imputable to wet snow on most of the plateau. Some isolated regions with higher σ^0 in the southern sector have been conservatively masked out in the 2011/2012 summer SECR prior to using this dataset for seasonal correction (Sect. 3.1.3).

Based on the analysis of the backscatter and of the SEC maps we manually outlined regions on the plateau which we considered prone to signal penetration in each DEM mosaic (Fig. S5). The outlining was performed manually in order to avoid areas on rough ice surfaces and on radar fore-slopes, where high σ^0 is not an indicator for signal penetration. We assigned a potential penetration height offset to each of these outlined regions according to their average σ^0. The offsets are based on the relationship between σ^0 and height offset between wet snow surfaces and dry snowpack derived from multi-seasonal TDM Raw DEMs of NPI (Supplement, Sect. S5). The extent of the areas likely affected by penetration is rather modest because we selected SAR scenes with wide-spread surface melt. Depending on the icefield and date, these cover from 0.9 to 2.3% of the total accumulation area. The penetration height offsets are taken into account in the error budget (Sect. 3.3.3).

3.2.2 Assessment of SRTM backscatter

The SRTM absolute and relative radiometric accuracy nominal values are 3 dB and 1 dB, respectively (Farr et al., 2007). The SRTMIMGR product provides the radar brightness β^0 at 1 arcsec corrected for flat earth for all the sub-swaths acquired during the mission. Lacking the orbital parameters of each acquisition, we coarsely removed the flat earth correction using the mid-look angle of each sub-swath, introducing this way an error up to ± 0.6 dB and computed the backscattering coefficient using the provided local incidence angle (θ_{loc}) mask as $\sigma^0 = \beta^0 \cdot \sin\theta_{\mathrm{loc}}$.

Figure S6 shows the arithmetic mean ($\bar{\sigma}^0$) and the standard deviation computed pixelwise from the sub-swath σ^0 images covering the icefields (4 to 7 stacked pixels are usually found). The measure of spread supports the interpretation of $\bar{\sigma}^0$. While σ^0 is similar for the HH and VV polarizations of the sub-swaths, variations of several dB are induced by the wide range of look angles (30° to 56°) at parity of snow conditions (Ulaby et al., 2014). The ERA Interim data show mean 850 hPa air temperatures between 3.3 and 3.8°C in February 2000 over the icefields, though temporal variations of LWC due to changing meteorological conditions cannot be excluded during the nine days of acquisition. On the other hand variations due to the diurnal temperature cycle are unlikely given the time of the Shuttle overpasses (Table S3).

Values of $\bar{\sigma}^0 < -22$ dB denoting the presence of wet snow are found on large sections of the plateaus. In the north-western part of SPI, a west-east gradient is visible (Fig. S6). Values of $\bar{\sigma}^0$ up to -18 dB are found in the 1800–1900 m range (the mean elevation of the plateaus) and up to -16 dB at elevations up to approximately 2300 m. These values may be attributed to wet snow with a rough surface (Nagler and Rott, 2000). Above 2300 m $\bar{\sigma}^0$ reaches up to -12 dB (excluding steep fore-slopes). Here nocturnal freezing of the upper snow layer is more likely, implying a displacement of the scattering phase centre in the order of decimetres (Floricioiu and Rott, 2001; Reber et al., 1987). This analysis was previously presented by Abdel Jaber (2016).

Considering the analysis of $\bar{\sigma}^0$, it can be concluded that the SRTM elevations are not affected by a bias due to C-band radar signal penetration except for few areas at high elevations with higher likelihood of penetration. These have been outlined (Fig. S6) and arssigned eoan estimated penetration hedight offset (cf. Supplement, Sect. S5) taken into account in the error budget (Sect. 3.3.3).

The good agreement of our volume change rates 2000 to 2012 over NPI with the results of Dussaillant et al. (2018) based on optical data supports the validity of our approach and the conclusions regarding signal penetration. Regarding possible penetration issues of the SRTM DEM, the analysis of Dussaillant et al. (2018) also indicates lack of penetration of the C-band SRTM radar signal into snow and firn except for a region above 2900 m a.s.l.

3.3 Uncertainty of SECR and mass balance

This section reports on the estimation of the different error sources affecting the SECR maps and the mass balance computed with the geodetic method.

3.3.1 Random error

The random error of each SECR sample σ_{SECR} was computed pixelwise as the quadrature sum of the random errors σ_h of the elevation samples of master and slave DEM, divided by the corresponding Δt in years:

$$\sigma_{\text{SECR}}(x,y) = \sqrt{\sigma_{h_m}(x,y)^2 + \sigma_{h_s}(x,y)^2}/\Delta t(x,y). \tag{3}$$

For TDM elevations the random error is given in the HEM raster, which expresses the interferometric standard error for each sample computed assuming a normally distributed error as (Rossi et al., 2010):

$$\sigma_h(x,y) = \sigma_\phi(x,y)\frac{h_a}{2\pi} \tag{4}$$

where h_a is the height of ambiguity and $\sigma_\phi(x,y)$ is the standard deviation of the interferometric phase which depends on the coherence and on the number of looks (Lee et al., 1994). The HEM does not include any systematic error components (phase unwrapping errors, etc.), these are discussed in Sect. 3.3.3. Concerning SRTM, the NASADEM also comes with a corresponding height error map providing σ_h. Where performed (section of SPI covered by the 2011/2012 summer SECR), the random error contribution of the pixelwise seasonal correction (Sect. 3.1.3) was also added in quadrature. The resulting random error maps for the two epochs are shown in Fig. S7.

3.3.2 Spatial correlation and spatial averaging

The standard error (SE) of a spatial average of several SECR samples is given by $\text{SE} = \sigma/\sqrt{N}$, where σ is the random error and N is the number of uncorrelated samples. To determine N the spatial correlation of the SECR maps was estimated by means of semivariograms. Two different regions of interest (ROIs), both verifying the assumptions of first- and second-order stationarity, were selected on ice-free terrain. ROI 1 features a relatively flat topography similar to the one of the CRs (Sect. 3.1.2), ROI 2 features varied slope and aspect distribution, simulating the icefield topography. The empirical omnidirectional semivariograms

obtained on the two ROIs for the TDM–SRTM and TDM–TDM SECR were furthermore fitted with an exponential model and are shown in Fig. S8. Among the model parameters reported in Table S6 the range of the semivariogram is an estimate of the correlation distance d_c of the SECR map, which was conservatively increased by ~ 40 %, to account for possible higher slopes on the averaged regions, among other factors. For the TDM–SRTM and TDM–TDM SECR maps we used, respectively, $d_c = 120$ m and $d_c = 60$ m to compute the standard error of the mean height offset on each CR (Sect. 3.1.2) and, respectively, $d_c = 200$ m and $d_c = 100$ m to compute the standard error of the mean SECR on the elevation intervals. For the estimation of N the theory of geostatistics was applied as in Rolstad et al. (2009) by integrating the exponential semivariogram model (they used a spherical model) in polar coordinates over a circular integration area A. The assumption of a negligible nugget (representing the uncorrelated component of the variance for the applied sampling interval) leads to the following expression for the number of uncorrelated samples N within A:

$$N = \left[-\frac{2}{9} \frac{A_c}{A} \left(3 \sqrt{\frac{A}{A_c}} e^{-3\sqrt{\frac{A}{A_c}}} + e^{-3\sqrt{\frac{A}{A_c}}} - 1 \right) \right]^{-1} , \tag{5}$$

where $A_c = \pi d_c^2$ is the correlation area. Equation (5) simplifies to $N = \frac{9}{2} \frac{A}{A_c}$ for the common case where $A \gg A_c$.

3.3.3 Systematic errors

Systematic errors are not reduced when spatial averaging is applied, they can hence have a significant impact on the mass balance of large areas. We defined four systematic error components.

1. An error linked to the coregistration to the reference DEM (Sect. 3.1.2) was defined for each Raw DEM and for the SRTM DEM of NPI and SPI as the interquartile range (IQR) of the all μ_r values (mean of Δh on CR r) used to estimate the height offset of that DEM. This error ranges between 0.04 m and 0.3 m. The corresponding systematic error component on the SECR ε_{reg} is obtained pixelwise as the quadrature sum of the coregistration errors of the master and slave DEMs scaled by Δt in years, similarly to Eq. (3).

2. To account for signal penetration we used the penetration height offsets assigned to critical regions on each DEM mosaic (Sect. 3.2) as local systematic errors, ranging between 1 m and 6 m according to σ^0, look angle and radar frequency (Sect. 3.2). Furthermore a bulk systematic error of 0.1 m was assigned to all remaining pixels above 1000 m a.s.l. to account for undetected regions and for possible small offsets on refrozen upper layer of snow and firn (Sect. 3.2). The systematic error component on the SECR ε_{pen} was obtained analogously to ε_{reg}.

3. An additional bulk systematic error was assigned to all glacier samples to account for unmodelled sources (e.g. residual GIA effects, residual tilts, unmasked local errors due to PU or layover, etc.). This source includes effects of the curvature-dependent SEC bias caused by the different resolution of the SRTM and TDM DEMs affecting small regions mostly at high elevation (Abdel Jaber, 2016). This additional error was set to 0.05 m for TDM, while for SRTM it was set to 0.2 m on SPI and 0.3 m on NPI to account for residual low-frequency elevation biases (Sect. 2.2). The systematic error component on the SECR ε_{add} was obtained analogously to ε_{reg}.

13

4. To compute the systematic error linked to the seasonal correction (Sect. 3.1.3), the previous three systematic error components ($\varepsilon_{\mathrm{reg}}$, $\varepsilon_{\mathrm{pen}}$ and $\varepsilon_{\mathrm{add}}$) were estimated separately for the summer 2011/2012 daily SECR and expressed in [m/d]. Here $\varepsilon_{\mathrm{add}}$ was increased by a factor of 1.5 to account for the different temporal coverage. All three components were summed in quadrature and conservatively further increased by a factor of 3.0 on extrapolated regions (north of SPI and NPI). A pixelwise scaling by the number of corrected days and by the appropriate Δt in years was applied, leading to a fourth systematic error component on the SECR, $\varepsilon_{\mathrm{seas}}$.

The total systematic error $\varepsilon(x, y)$ of each SECR sample was obtained pixelwise as (omitting (x, y) for compactness):

$$\varepsilon(x, y) = \sqrt{\varepsilon_{\mathrm{reg}}^2 + \varepsilon_{\mathrm{pen}}^2 + \varepsilon_{\mathrm{add}}^2 + \varepsilon_{\mathrm{seas}}^2}. \tag{6}$$

The mean values of $\varepsilon(x, y)$ and of its components for the four SECR maps are reported in Table S7.

3.3.4 Geodetic mass balance error

The geodetic method was applied to estimate the average SECR on separate elevation bins and the corresponding volume and mass change rates. The total error of the mean SECR on elevation bin b was computed by summing in quadrature the mean systematic error $\overline{\varepsilon}_b$ on bin b and the standard error SE_b of the spatial average on bin b (which is generally negligible compared to $\overline{\varepsilon}_b$), obtained as:

$$\mathrm{SE}_b = \sqrt{\frac{\overline{\sigma_{\mathrm{SECR}}^2}}{N_b}}. \tag{7}$$

where N_b is computed according to Eq. (5).

In the geodetic method the mean of the valid SECR samples of bin b is extrapolated to the unsurveyed area of the bin. On such gaps the total error was increased by a factor of 1.5 when computing the mass balance of a single glacier basin and a by factor of 3.0 when computing it on the entire icefield, to account for the across-basin variability of the SEC, particularly at lower elevations.

To calculate the volume change rate a 2 % error was assigned to the glacier area obtained from the updated outlines (Sect. 2.3). This value is higher than the RGI error suggested by Pfeffer et al. (2014) and in line with the empirical findings of Paul et al. (2013). The uncertainty of the density used for the volume to mass change rate conversion was set to $\pm 36\ \mathrm{kg\,m^{-3}}$ (4 %). This number is based on an estimated uncertainty of $\pm 17\ \mathrm{kg\,m^{-3}}$ for density in the ice areas and $\pm 54\ \mathrm{kg\,m^{-3}}$ in the firn areas. In Sect. 4 the average SECR and VCR errors estimated for each bin are visualized graphically on the hypsometric plots, while the errors estimated for the entire icefields and for the individual glaciers are reported in the results tables.

4 Results

The SECR maps of NPI and SPI after seasonal correction are shown in Fig. **??** for the two main epochs 2000–2012 (epoch 1) and 2012–2016 (epoch 2) along with the TDM DEM mosaic of 2012 used as hypsometric reference to analyze the elevation

dependence. Unsurveyed areas in the SECR maps are relatively small and geographically evenly distributed, with the exception of the eastern margin of NPI in 2012–2016 because of layover caused by the steep incidence angle of scenes 6 and 7. In Table **??** the SECR, the volume change rate (VCR), the mass balance and the contribution to sea level rise are specified for the entire icefields. Table **??** provides SECR and VCR for NPI glaciers larger than 2 km^2, Table **??** for SPI glaciers larger than 35 km^2 and Table S8 in the Supplement for SPI glaciers with area between 35 km^2 and 9 km^2. The tables report also the measured basin areas (based on the updated RGI glacier outlines) and the percentage of SECR coverage for the two epochs. The reference hypsometry and the distribution of unsurveyed areas are shown in Figs. S10 and S11 for NPI and SPI, respectively. The altitude dependence of SECR and VCR is shown in Fig. **??** for NPI and its main glaciers and in Fig. **??** for SPI and its main glaciers, while plots for additional glaciers are reported in Figs. S12 and S13. SECR and VCR are assembled in 50 m elevation bins using the surface of the 2012 TDM DEM as reference. The SECR averaged over each glacier basin is visualized in Fig. S9 together with the 2012 TDM DEM average surface elevation.

NPI shows a similar pattern of elevation change during the two epochs, with the highest rates of thinning on the lowest sections of the glacier tongues, gradually decreasing up-glacier. Equilibrium state is reached on average at about 1800 m elevation (Fig. **??**). On the south-western sector of the icefield and on San Quintin Glacier the thinning rates at elevations below 1200 m are slightly higher than in the northern and eastern sectors. All glaciers with an area larger than 20 km^2 show volume losses during both epochs except Leones Glacier revealing a modest increase in ice volume (Table **??**). The volume loss rate of NPI increased from epoch 1 (VCR = −4.26 km^3 a^{-1}) to epoch 2 (VCR = −5.60 km^3 a^{-1}). The three largest glaciers (San Quintin, San Rafael, Steffen) account for 50 % of the NPI volume loss during epoch 1 and for 48 % during epoch 2. During both epochs the highest SECR at basin scale was observed on HPN 1 (VCR = −2.50 m a^{-1} and −3.25 m a^{-1}, respectively). On all glaciers larger than 20 km^2, except Arco Glacier and Leones Glacier (with positive mass balance), the loss rates were higher during epoch 2. San Quintin Glacier (Fig. **??**, Fig. **??**) shows the highest increase in volume loss (VCR = −0.60 km^3 a^{-1} and −0.92 km^3 a^{-1}). On San Rafael Glacier the loss rate increased slightly from epoch 1 to epoch 2 (VCR = −0.81 km^3 a^{-1} and −0.87 km^3 a^{-1}), but the loss pattern changed (Fig. **??**, Fig. **??**). On the terminus below about 800 m a.s.l. the rate of surface lowering decreased, whereas in the upper reaches loss rates became larger.

On SPI the spatial pattern of surface elevation change is more complex and the temporal trend is less uniform. Contrary to NPI, the volume loss of SPI decreased from epoch 1 (VCR = −14.87 km^3 a^{-1}) to epoch 2 (VCR = −11.86 km^3 a^{-1}). The three glaciers Upsala, Jorge Montt and Viedma account for 45 % of the SPI volume loss in epoch 1 and for 58 % in epoch 2. On Upsala Glacier the rate of surface lowering decreased on the terminus from epoch 1 to epoch 2 (Fig. **??**) associated with a slowdown of calving velocity. The losses increased on Jorge Montt Glacier (Fig. **??**) and on Viedma Glacier. Very high loss rates are observed on the lower sections of the Jorge Montt terminus, with SECR (for a 50 m elevation bin) of −16.7 m a^{-1} during epoch 1 and −25.6 m a^{-1} during epoch 2. The loss rates decrease gradually up-glacier, but the main sections of the accumulation area of these glaciers, up to elevations of 1800 m to 2000 m, were affected by downwasting during both epochs (Fig. **??**).

Other glaciers with volume loss rates > 0.5 km^3 a^{-1} are located in the northern sector of SPI (O'Higgins, Bernardo, Greve, Tempano, Occidental), in the centre/west sector of the icefield (HPS 12), and in the south-west (Tyndall Glacier). Average

thinning rates up to 40 m a^{-1} are observed on the terminus of HPS 12 Glacier during epoch 1. The HPS 12 terminus, flowing through a deep, narrow fjord, retreated by almost 5 km between 2000 and 2012 and by 4 km between 2012 and 2015. In epoch 2 the average SECR and VCR could not be estimated reliably because of significant gaps on the terminus in the 2015 DEM due to phase unwrapping errors (Fig. **??**b), nevertheless thinning rates higher than 40 m a^{-1} could be observed at the 2012 front. Next to HPS 12 the highest loss rates at basin scale are observed on Jorge Montt Glacier (SECR = −4.01 m a^{-1} and −4.95 m a^{-1} during the two epochs) and on Upsala Glacier (SECR = −3.33 m a^{-1} and −3.04 m a^{-1}).

The only glacier with positive mass balance in both epochs is Pio XI Glacier, showing a significant increase of VCR from 0.52 km^3 a^{-1} in epoch 1 to 1.26 km^3 a^{-1} in epoch 2 (Fig. **??**). SEC rates in the elevation zones up to 1500 m a.s.l. were positive during both epochs. During epoch 1 the elevation zone between 100 m and 400 m a.s.l. accounted for the main contribution to the total gain in ice mass. During epoch 2 an additional source of significant mass gain was the elevation zone between 1000 m and 1500 m on the ice plateau (Fig. **??**).

On the western sector south of HPS 12 (49.6° S) and on the eastern sector south of Upsala Glacier (49.9° S) the average loss rates are smaller than on the northern sector, but all glaciers covering areas > 35 km^2 and the majority of smaller glaciers show negative SECR during epoch 1 (Table **??** and S13). On the main ice plateau the surface elevation was either stable or the SECR was slightly negative during epoch 1, becoming slightly positive during epoch 2. During epoch 2 the mass balance of several glaciers of the southern sector switched from negative to slightly positive values. However, the termini of the majority of glaciers were thinning during both epochs. The largest contributors to the SPI mass deficit in the southern sector during epoch 1 were Tyndall Glacier (VCR = −0.79 km^3 a^{-1}) and Grey Glacier (VCR = −0.44 km^3 a^{-1}). On both glaciers the volume loss rate decreased significantly during epoch 2, on Tyndall Glacier (VCR = −0.48 km^3 a^{-1}) mainly due to decrease of losses above 700 m a.s.l. (Fig. **??**) and on Grey Glacier (VCR = −0.07 km^3 a^{-1}) at all elevations (Fig. **??**, Fig. **??**). Other glaciers with distinctly different hypsometric VCR between the two epochs are Penguin, Europa, Amalia, HPS 41 (Fig. S13).

Figure **??** shows a map of daily SECR on SPI during summer 2011/2012 based on DEM differencing spanning the periods 18/12/2011 to 26/3/2012 (99 days), 7/12/2011 to 15/3/2012 (99 days) and 29/12/2011 to 31/1/2012 (33 days). During summer the signal of surface lowering in the accumulation areas is mainly related to firn densification and melting of the top snow layers (Rivera, 2004). On the firn plateau, at elevations ≥ 1200 m, the average SECR in summer 2011/2012 was about −0.03 m d^{-1} (blue curve in Fig. S3). In the ablation areas ice melt and dynamic downwasting (varying from glacier to glacier) are the main factors. High loss rates (SECR <∼ −0.08 m d^{-1}) refer to areas that are subject to significant dynamic thinning, such as the lower terminus of Upsala and Viedma glaciers. Average summer melt rates for ice on the lower terminus of Perito Moreno Glacier (at 300 m altitude) are about 0.05 m d^{-1} (Stuefer et al., 2007). On a glacier in balanced state surface lowering due to melt is in summer partly compensated by uplift due to emergence.

The reported volume change and mass balance do not include subaqueous ice volume changes. Subaqueous losses are negligible in respect to the mass change of NPI since there are no large frontal retreats on water bodies. On SPI the main glaciers, and also many smaller ones, terminate in proglacial lakes or in oceanic fjords. For the main retreating glaciers of SPI Abdel Jaber (2016) estimated the subaqueous ice VCR at −0.73 ± 0.22 km^3 a^{-1} for the period 2000 to 2011/2012. This number is obtained by measuring or estimating various parameters at the glacier front, including the glacier width, the water depth, the

freeboard height on the two dates and the retreat distance. A bulk error of 30 % is assigned to the total subaqueous volume change rate, accounting also for unsurveyed glaciers. For the basal cross-section at the calving front the shape of a semi-ellipse is assumed except for four glaciers for which bathymetric data is available enabling more precise estimates. For these glaciers a bulk error of 20% is assumed for the subaqueous volume changes, amounting for the whole period to -2.80 ± 0.56 km^3 on the main front of Upsala Glacier, -0.68 ± 0.14 km^3 on Jorge Montt Glacier, -0.59 ± 0.12 km^3 on Tyndall Glacier and -0.05 ± 0.01 km^3 on Ameghino Glacier. The estimated subaqueous volume changes for the period 2000–2011/2012 are reported in Table S9, together with the frontal retreat distance.

5 Discussion

5.1 Spatial and temporal pattern of surface elevation and glacier volume change

Patagonian glaciers and icefields experienced area retreat and shrinkage since the Little Ice Age which accelerated during recent decades associated with tropospheric warming (Davies and Glasser, 2012). Our estimate of mass loss for both icefields during the period 2000 to 2016 is equivalent to 0.047 ± 0.003 mm a^{-1} eustatic sea level rise. This corresponds to 6 % of the ensemble mean contribution to sea level rise of glaciers and ice caps for the period 2005–2016 of 0.74 ± 0.18 mm a^{-1}, based on global mass balance estimates from various sources (Cazenave et al., 2018). Between epoch 1 (2000–2012) and epoch 2 (2012–2016) the rate of mass loss of SPI and NPI combined decreased by 9 % with a contrasting temporal trend between the two icefields. The spatially detailed maps of SECR during the two subsequent epochs, derived from bistatic InSAR DEMs, provide a sound basis for studying the heterogeneous pattern of glacier response on NPI and SPI.

Regarding the ice bodies at large, on NPI the average loss rate increased by 31 % from epoch 1 to epoch 2 (VCR = -4.26 ± 0.20 km^3 a^{-1} and -5.60 ± 0.74 km^3 a^{-1}, respectively). This was reverse on SPI where the loss rate decreased by 20 % (VCR = -14.87 ± 0.52 km^3 a^{-1} and -11.86 ± 1.99 km^3 a^{-1}, respectively). Reasons for the different behaviour are temporal changes of calving velocities, in particular on SPI, as well as a north-south gradient of air temperature increase in epoch 2 compared to epoch 1. Air temperatures, based on the European Centre for Medium-Range Weather Forecasts Interim Re-Analysis (ERA-Interim) (Dee et al., 2011; Berrisford et al., 2011) show for the ERA grid point 47.25° S, 73.5° W (NPI) in 850 hPa a mean annual temperature of +1.9 °C during the period 2000–2011 and +2.3 °C during 2012–2015. The corresponding values at the grid point 50.25° S, 73.5° W (southern SPI) are: +0.7 °C and +0.8 °C. The temperature difference between the two epochs was slightly larger during the main ablation period (1 November to 31 March): +4.1 °C (summer 2000/2001 to 2011/2012) and +4.8 °C (summer 2011/2012 to 2015/2016) on the NPI grid point, +2.4 °C and +2.7 °C on southern SPI. The NCEP/NCAR Reanalysis 850 hPa mean temperature (Kalnay et al., 1996) is about 1 °C lower, but shows a similar temporal and spatial trend. Over an area extending from 72.75° W to 74.25° W, 48.00° S to 51.75° S, covering SPI, the mean annual precipitation, derived from ERA Interim data, was slightly higher (8.4 %) in epoch 1 than in epoch 2 (Langhamer, 2017; Langhamer et al., 2018).

A main factor for the increased mass losses during epoch 2 on NPI is the higher air temperature compared to epoch 1, in particular during the main ablation period. Assuming a degree-day factor of 0.7 cm d^{-1} on ice areas (Stuefer et al., 2007), the melt loss for an increase of surface temperature by 0.7 °C during November to March corresponds to an additional loss of 0.74

m water equivalent. The hypsometric plot for the whole icefield shows changes of SECR by about $-0.7\,\mathrm{m\,a^{-1}}$ up to elevations of 1200 m a.s.l., indicating increased melt losses during epoch 2 not only on glacier termini but also on lower sections of the NPI plateau. At higher elevations the rate of surface lowering in both epochs, including the additional contribution during epoch 2, decreases gradually with elevation, reaching balanced state at about 1800 m in epoch 1 and about 2100 m in epoch 2 (Fig. **??**). On NPI surface melt is the dominating process for mass depletion. During the period 2000 to 2009 the ice export due to calving amounted to about 20 % of the annual mass depletion by surface melt (Schaefer et al., 2013).

On lower sections of the main calving glaciers temporal variations of flow velocities are a main factor for the differences in SECR during the two epochs. In order to support the interpretation of differences in SECR between the two epochs, we derived maps of surface velocity gridded at 50 m for main glaciers from TerraSAR-X 11-day repeat pass data on various dates between 2010 and 2016, applying the offset tracking technique. The uncertainty of the velocity magnitude of these products is $0.05\,\mathrm{m\,d^{-1}}$(Wuite et al., 2015). Plots of velocities along central flowlines, extracted from the velocity maps, are shown in Fig. **??** for Jorge Montt, Pio XI, Upsala and Viedma glaciers.

Flow velocities near the calving front of San Rafael Glacier reached magnitudes in excess of $18\,\mathrm{m\,d^{-1}}$ in April 2007 (Willis et al., 2012a), dropping to $16\,\mathrm{m\,d^{-1}}$ in May 2012 (Abdel Jaber et al., 2014). Mouginot and Rignot (2015) report for the velocity at 10 km from the ice front a temporal peak in 2005 and a decrease by about 20 % until 2014. The drop in velocity between epoch 1 and 2 is reflected in the hypsometric curve of SECR, showing reduced loss rates below 800 m elevation during epoch 2 (Figs. **??** and **??**). San Quintin Glacier, the largest glacier of NPI, reaches its maximum speed of about $3\,\mathrm{m\,d^{-1}}$ 30 km from the front (Abdel Jaber et al., 2014; Mouginot and Rignot, 2015). Our analysis of TerraSAR-X data shows between May 2012 and June 2016 on the terminus a mean increase in velocity by 10 %. However, this caused only a minor additional increase of surface lowering (Fig. **??**) because for this glacier the ice export due to calving accounts only for a very small part of total mass turnover (Schaefer et al., 2013).

On SPI calving fluxes play a larger role for mass turnover than on NPI. This is reflected in the change of the average hypsometric curve of SECR of the icefield between the two epochs (Fig. **??**). In spite of similar air temperatures during epoch 2 the average rate of surface lowering decreased at elevations below 400 m. Between 400 m and 1000 m elevation the differences between the two epochs are very small. On the ice plateau, between 1000 m and 2000 m, the loss rate decreased slightly, mainly brought about by minor changes on the southern sector of the icefield. Local increase in snow accumulation may play a role.

For six glacier basins the VCR between the two epochs changed by more than $+0.2\,\mathrm{km^3\,a^{-1}}$, summing up to a combined decrease of volume losses by $2.20\,\mathrm{km^3\,a^{-1}}$ (Table **??**). The change of VCR from epoch 1 to epoch 2 amounted for Pio XI Glacier to $+0.74\,\mathrm{km^3\,a^{-1}}$, for Grey & Dickson to $+0.37\,\mathrm{km^3\,a^{-1}}$, for Upsala & Cono to $+0.33\,\mathrm{km^3\,a^{-1}}$, for Tyndall to $+0.30\,\mathrm{km^3\,a^{-1}}$, for Europa to $+0.24\,\mathrm{km^3\,a^{-1}}$, for Penguin to $+0.22\,\mathrm{km^3\,a^{-1}}$.

The behaviour of Pio XI Glacier, with frontal advance and positive mass balance since many years is opposed to the general trend of SPI glaciers. The recent frontal advance trend started at the northern section of the terminus in 2006 and at the southern section in 2000 (Wilson et al., 2016). Between 2000 and 2014 a slowdown of velocity was observed on the southern section of the terminus (Mouginot and Rignot, 2015; Wilson et al., 2016). The slowdown went on until 2016, whereas the velocity of

the northern section more than doubled between 2013 and 2016 (Fig. **??**). Bathymetric data show shallow water with ridges running across the fjord at the present position of the ice front Dowdeswell and Vásquez (2013). This impedes calving at the southern ice front, causing during epoch 1 a main increase of surface elevation on the southern section, later on shifting towards the northern section that calves into Lago Greve (Fig. **??**).

On Upsala Glacier the front retreated by 4 km between 2000 and 2014. The calving velocity reached a maximum in 2009/2010 (Abdel Jaber et al., 2012; Mouginot and Rignot, 2015) and decreased significantly afterwards, dropping from 8 md^{-1} in March 2011 to 5.9 md^{-1} in August 2014 and 4.8 md^{-1} in August 2016 (Fig. **??**). This caused a major decrease in the thinning rate of the lower terminus during epoch 2 (Fig. **??**).

The hypsometric curves of Grey and Tyndall glaciers show little change in SECR on the lower terminus close to the calving front and decreasing loss rates in the upper reaches of the terminus and in the accumulation area, an indication for surface mass balance as main cause for the change in SECR (Fig. **??**). This is in line with TerraSAR-X surface velocity results between December 2011 and August 2016 showing only modest changes near the ice front and slowdown upstream. On Tyndall Glacier the velocity on the central flowline 0.5 km from the front was 0.96 md^{-1} in December 2011, 0.88 md^{-1} in October 2013 and 0.96 md^{-1} in August 2016. On Grey Glacier at the central flowline 3 km from the front, where the glacier splits into three branches, the velocity was 1.13 md^{-1} in December 2011, 1.11 md^{-1} in October 2013 and 1.02 md^{-1} in April 2016. Further upstream the velocity decreased by about 20 % between 2011 and 2016 on both glaciers. Weidemann et al. (2018) computed the surface mass balance of both glaciers and estimated the calving flux as residual of mean surface mass balance and geodetic mass balance over the period 2000 to 2014, pointing out that ice loss by surface ablation exceeds ice loss by calving. On Europa and Penguin, featuring steep narrow tongues, the SECR switched from slightly negative values to slightly positive values on the ice plateau above 1000 m elevation, indicating also a change in surface mass balance.

There are three glaciers with major increase of losses during epoch 2 (VCR becoming more negative by ≥ 0.2 $km^3 a^{-1}$): the change of VCR for Jorge Montt is -0.36 $km^3 a^{-1}$, for Viedma -0.28 $km^3 a^{-1}$, for Bernardo -0.20 $km^3 a^{-1}$. Jorge Montt Glacier experienced a frontal retreat by 11 km between 1990 and 2011 (Rivera et al., 2012) and a further retreat by 2 km until 2016. The hypsometric profile shows high loss rates on the terminus at elevations up to 1000 m, with losses increasing during the second epoch (Table **??**, Fig. **??**) associated with major flow acceleration between 2007 and 2014 (Mouginot and Rignot, 2015). Figure **??** shows flow acceleration 2010 to 2015/2016 extending 30 km up-glacier. On Viedma Glacier the increased mass loss during epoch 2 is caused by a major increase of the thinning rate on the glacier terminus below 1000 m elevation, an indication for changes in dynamic downwasting. This in accordance with a increase of ice velocity between 2010 and 2016 on the glacier terminus, notably in the lowest 5 km (Fig. **??**). The calving velocity increased from 2 md^{-1} in August 2010 to 3.8 md^{-1} in August 2016.

The heterogeneous spatial pattern of elevation change on the two icefields and its temporal evolution are results of complex interdependencies between surface mass balance, responding directly to climate change signals, and effects of flow dynamics. Differences in surface elevation change and mass balance between individual glaciers and their temporal trends are particularly pronounced on SPI, where the calving fluxes represent a main component of mass turnover for most glaciers. The elevation

dependence of the SEC reveals that ice dynamics exerts a main control on topography not only on the glacier tongues, but also on parts of the main ice plateau.

5.2 Comparison with previous estimates

A comparison of published results on volume change rates of SPI and NPI is reported in Table S10 for different epochs between 1968 and 2017, based on various methods including differencing of optical and/or interferometric DEMs and gravimetric time series of the GRACE mission. Similar comparisons are found in Malz et al. (2018) and Foresta et al. (2018). Our results are in line with geodetic mass balance results of NPI and SPI published by other authors, which suggest an overestimation of the mass losses retrieved from gravimetric time series such as those found in Chen et al. (2007), Ivins et al. (2011) and Jacob et al. (2012), the latter referring to Patagonia in general.

Our result for NPI during epoch 1 (VCR = -4.26 ± 0.20 km^3 a^{-1}) complies with the numbers reported by Abdel Jaber (2016) for the period 2000 to 2014 (-4.40 ± 0.13 km^3 a^{-1}) and Willis et al. (2012a) for 2000 to 2011 (-4.06 ± 0.12 km^3 a^{-1}), the latter based on SRTM and ASTER DEMs. Willis et al. (2012b) recomputed their previous estimate applying a 2 m offset to the SRTM DEM to account for signal penetration which results in larger losses (VCR = -4.9 ± 0.3 km^3 a^{-1}). This correction is not comprehensible given the wet status of the snow surface during the summer acquisition of SRTM as evident from the backscatter data (Sect. 3.2.2, and Abdel Jaber (2016)). Braun et al. (2019) report for NPI a VCR -4.65 ± 0.17 km^3 a^{-1} over the period 2000 (SRTM data) to 2011/2015 (TDM data).

Our VCR for epoch 1 is slightly lower than the results of Dussaillant et al. (2018) who applied two methods: differencing of SPOT and SRTM DEMs (VCR = -4.55 ± 0.41 km^3 a^{-1}) and derivation of temporal elevation trends from ASTER DEM time series (VCR = -4.72 ± 0.34 km^3 a^{-1}). Our hypsometric curve of SEC shows up to 2800 m of elevation a similar behaviour as their ASTER_trend results, although with slightly lower losses at most elevations. Above 1000 m Dussaillant et al. (2018) report 35 % and 22 % of unsurveyed area for the SPOT-SRTM analysis and ASTER_trend respectively, mostly due to the lack of contrast or the presence of clouds in the optical stereo images. For the same elevation band the unsurveyed area in our 2000–2012 SECR map of NPI is 6 %. On glaciers larger than 100 km^2 the SEC rates with both methods applied by Dussaillant et al. (2018) agree with our results within error bars. On two medium-sized glaciers, Exploradores (86 km^2) and Grosse (67 km^2), the average SECR of their two methods differs by more than 1.0 m a^{-1}, their ASTER_trend being ~ 0.8 m a^{-1} higher than our SECR and ~ 0.6 m a^{-1} higher than those of Willis et al. (2012a).

On SPI Willis et al. (2012b) estimate a VCR of -21.2 ± 0.5 km^3 a^{-1} for the period 2000–2011, a much larger value compared to the value reported here for epoch 1 (VCR = -14.87 ± 0.52 km^3 a^{-1}) and to that of Abdel Jaber (2016) for 2000–2011/2012 (VCR = -14.59 ± 0.37 km^3 a^{-1}). The discrepancy largely exceeds the 10 % VCR contribution they attribute to the 2 m correction for signal penetration in the SRTM DEM.

Malz et al. (2018) present SECR maps and mass balance of SPI for the period 2000–2015 based on SRTM and several TDM DEMs of December 2015. We used the same raw data at the end of our epoch 2. They do not account for missing summer days and report a VCR of -13.2 ± 3.6 km^3 a^{-1}. Scaling our VCR results over the two epochs and accounting for the missing summer days in order to cover a period of 16 years, from mid-February 2000 to mid-February 2016, we obtain -14.1 ± 0.9

km^3 a^{-1}. The difference can probably be explained by the missing 48 to 76 summer days required for spanning a full period of 16 years. Applying the method of Sect. 3.1.3 for the missing summer days, we obtain an icefield-wide average SECR value of -0.12 m a^{-1}, corresponding to a VCR of -1.5 km^3 a^{-1}, which is not taken into account by Malz et al. (2018). For the southern sector of SPI Malz et al. (2018) show SECR maps and hypsometric curves for the periods 2000–2012 and 2012–2015, based on the same TDM raw data used in this study (scenes 7/8 and 13/14). The absence of a correction for 53/59 summer days at the end of the 4-year period leads to lower loss rates compared to our numbers for epoch 2.

Average SEC rates for single glaciers are reported by Willis et al. (2012b) and Malz et al. (2018). On several main glaciers, including Bernardo, Tempano, Occidental, Greve, Chico, Europa and Guilardi glaciers, a direct comparison is not possible because of different glacier outlines. Among main glaciers with similar area our SECR estimates are in general lower than those of Willis et al. (2012b). Among glaciers > 200 km^2, average SEC rates deviating by more than -1.0 m a^{-1} from our results are reported for Tyndall, Pio XI and Perito Moreno glaciers.

Foresta et al. (2018) compute the geodetic mass balance of NPI and SPI for six glaciological years between 2011 and 2017 from SEC maps using swath processed CryoSat-2 (CS2) interferometric data with sub-kilometre spatial resolution. The acquisitions dates vary spatially for different pixels. The authors explain that seasonality biases are avoided due to the regular flight path of CS2 ensuring data acquisition within each pixel at the same epochs in each glaciological year. The data coverage is relatively poor (46 % for NPI, 50 % for SPI), in particular on lower sections of glacier tongues. Termini of several main glaciers are not covered at all and the SECR data appear to be relatively noisy. To fill data gaps hypsometric average models are applied, using the values of polynomials (degree 1 to 3) fitted to the observed hypsometric SECR. This is performed for NPI at large and for SPI separately for six of the main glaciers and two large sub-regions each of which comprises many glaciers of different size and physiographic features. Therefore the resulting maps of SECR do not reflect the complexity and spatial variability of SECR derived from high resolution geodetic data, particularly at lower elevations.

A comparison between VCR estimates of Foresta et al. (2018) and our results for 2012–2016 is provided in Table S11. The two data sets do not cover exactly the same period. The ERA Interim 850 hPa data over NPI and SPI show for the average air temperature of the main ablation period (November to March) 2011 to 2017 an agreement within 0.1 °C compared to 2012–2016, suggesting similar rates of surface melt during the two epochs. Foresta et al. (2018) report a mass balance of -6.79 ± 1.16 Gt a^{-1} for NPI and -14.50 ± 1.60 Gt a^{-1} for SPI using 900 ± 125 kg m^{-3} for volume-to-mass conversion. This corresponds to a VCR of -7.54 ± 0.75 km^3 a^{-1} and -16.11 ± 1.43 km^3 a^{-1}, respectively. These numbers for volume loss are significantly higher than our results for epoch 2 in all sub-regions, being overall 35 % higher for NPI and 36 % for SPI. Foresta et al. (2018) show also time series of cumulative mean observed elevation change for the nine sub-regions. For NPI and five sub-regions of SPI the plots show in some years minima of the annual elevation during mid-winter. This is not compatible with both the annual cycle of surface mass balance and the seasonal variation of flow velocities on glacier tongues showing a trend for higher velocities in summer compared to winter (Stuefer et al., 2007; Minowa et al., 2017).

6 Conclusions

We report on a detailed study focussing on the climate-sensitive Northern and Southern Patagonian icefields, where high resolution maps of surface elevation change were obtained for the epochs 2000–2012 and 2012–2016 from bistatic InSAR DEMs allowing to derive the total net mass balance of most of the glacier basins. We rely on a re-processed version of the SRTM C-band DEM featuring improved absolute height calibration and on a series of TanDEM-X Raw DEMs, processed with a robust phase unwrapping method, leading to almost complete coverage including narrow glaciers and high altitudes. Significant effort was dedicated to reduce systematic errors, especially critical for the mass balance of vast regions: a precise coregistration of the DEMs was performed, seasonal biases due to gaps in the full annual cycle were corrected based on a complementary TDM summer SEC map, the backscatter coefficient of all acquisitions (including SRTM) was analysed to assess signal penetration. A comprehensive uncertainty estimation including all main error sources of the SEC maps and of the mass balance was also performed.

A similar pattern of elevation change is found on NPI for the two epochs, with lowering on most of the termini and well into the main ice plateau with increased loss rates during epoch 2. Being mass depletion mainly driven by surface melt on NPI, this trend is likely due to higher average air temperatures during epoch 2. The estimated volume change rate increased by 31 % from -4.26 ± 0.20 km^3 a^{-1} in epoch 1 to -5.60 ± 0.74 km^3 a^{-1} in epoch 2.

On SPI the spatial pattern and the temporal trend of SECR are more complex. For 63 % of the glaciers larger than 35 km^2 in area the loss rate decreased or turned into positive values from epoch 1 to epoch 2, whereas for 37 % the loss rates increased. The overall volume change rate decreased by 20 % from -14.87 ± 0.52 km^3 a^{-1} during epoch 1 to -11.86 ± 1.99 km^3 a^{-1} during epoch 2. The only glacier with positive mass balance in both epochs is Pio XI Glacier with an increase of the volume change rate from 0.52 ± 0.04 km^3 a^{-1} to 1.26 ± 0.25 km^3 a^{-1}. The more complex behaviour of SPI glaciers is caused by the higher relevance of calving fluxes as a source of mass turnover in which the effect of ice dynamics on surface elevation changes extends to the main plateau. Different temporal trends between individual glaciers are commonly associated with opposing trends in calving velocities. On the accumulation areas south of $\sim 49.5°$ S the SECR was either stable or slightly negative during epoch 1, turning to slightly positive in epoch 2. Air temperature remained relatively stable in the south of SPI, meaning a north-south gradient was present. This, coupled with a possible local increase in snow accumulation may be the cause of the decreased loss rates at elevations above 1000 main ice plateau. Significant frontal retreat was observed on SPI during epoch 1, Abdel Jaber (2016) reported a coarse estimation of subaqueous volume change of -0.73 ± 0.22 km^3 a^{-1} for the period 2000–2011/2012.

The eustatic sea level rise contribution of both icefields, excluding subaqueous changes, was estimated to be 0.048 ± 0.002 mm a^{-1} in epoch 1 and 0.043 ± 0.005 mm a^{-1} in epoch 2. Behind these numbers lies a complex interplay between surface mass balance, responding directly to climate change, and ice flow dynamics, mechanisms which regulate the heterogeneous spatial pattern and temporal evolution of the SEC on NPI and SPI.

This study confirms the potential of bistatic InSAR and particularly of the TanDEM-X mission for accurate, detailed and almost gapless mapping of surface elevation changes of large icefields even for small basins and tongues. We recommend the use of TanDEM-X data—with an appropriate coregistration and care for radar signal penetration—to map SEC of all types of glaciers, as recently shown also in the northern Antarctic Peninsula (Rott et al., 2018). We hope that our results will encourage the development of remote sensing missions capable of repeated bistatic InSAR observations allowing regular worldwide SEC mapping and mass balance estimations with improved temporal sampling.

Data availability. The SECR maps will be made available upon publication of the final version on http://cryoportal.enveo.at

Author contributions. WAJ, HR and DF conceived and designed the study. WAJ selected and processed the TanDEM-X DEMs and produced the results and their visualization. JW processed updated TerraSAR-X ice flow velocities. HR devised the seasonal correction and performed the glaciological analysis of the results. WAJ prepared the manuscript with contributions from all co-authors.

Competing interests. The authors declare that they have no conflict of interest.

References

Abdel Jaber, W.: Derivation of mass balance and surface velocity of glaciers by means of high resolution synthetic aperture radar: application to the Patagonian Icefields and Antarctica, Dissertation, Technische Universität München, http://elib.dlr.de/109075/, 2016.

Abdel Jaber, W., Floricioiu, D., Rott, H., and Eineder, M.: Dynamics of fast glaciers in the Patagonia Icefields derived from TerraSAR-X and TanDEM-X data, in: 2012 IEEE International Geoscience and Remote Sensing Symposium (IGARSS), pp. 3226–3229, 2012.

Abdel Jaber, W., Floricioiu, D., and Rott, H.: Glacier dynamics of the Northern Patagonia Icefield derived from SRTM, TanDEM-X and TerraSAR-X data, in: 2014 IEEE International Geoscience and Remote Sensing Symposium (IGARSS), pp. 4018–4021, 2014.

Åström, J. A., Vallot, D., Schäfer, M., Welty, E. Z., O'Neel, S., Bartholomaus, T., Liu, Y., Riikilä, T. I., Zwinger, T., Timonen, J., and Moore, J. C.: Termini of calving glaciers as self-organized critical systems, Nature Geoscience, 7, 874–878, 2014.

Benn, D. I., Warren, C. R., and Mottram, R. H.: Calving processes and the dynamics of calving glaciers, Earth-Science Reviews, 82, 143–179, 2007.

Berrisford, P., Dee, D., Poli, P., Brugge, R., Fielding, K., Fuentes, M., Kållberg, P., Kobayashi, S., Uppala, S., and Simmons, A.: The ERA-Interim archive, version 2.0, ERA Report Series, p. 23, https://www.ecmwf.int/en/elibrary/8174-era-interim-archive-version-20, 2011.

Braun, M. H., Malz, P., Sommer, C., Farías-Barahona, D., Sauter, T., Casassa, G., Soruco, A., Skvarca, P., and Seehaus, T. C.: Constraining glacier elevation and mass changes in South America, Nature Climate Change, 9, 130, 2019.

Bravo, C., Quincey, D., Ross, A., Rivera, A., Brock, B., Miles, E., and Silva, A.: Air Temperature Characteristics, Distribution, and Impact on Modeled Ablation for the South Patagonia Icefield, Journal of Geophysical Research: Atmospheres, 124, 907–925, 2019.

Breit, H., Lachaise, M., Balss, U., Rossi, C., Fritz, T., and Niedermeier, A.: Bistatic and interferometric processing of TanDEM-X data, in: EUSAR 2012; 9th European Conference on Synthetic Aperture Radar, pp. 93–96, 2012.

Brown, C. G., Sarabandi, K., and Pierce, L. E.: Validation of the shuttle radar topography mission height data, IEEE Transactions on Geoscience and Remote Sensing, 43, 1707–1715, 2005.

Carabajal, C. C. and Harding, D. J.: SRTM C-band and ICESat laser altimetry elevation comparisons as a function of tree cover and relief, Photogrammetric Engineering and Remote Sensing, 72, 287–298, 2006.

Cazenave, A., Meyssignac, B., Ablain, M., Balmaseda, M., Bamber, J., Barletta, V., Beckley, B., Benveniste, J., Berthier, E., Blazquez, A., et al.: Global sea-level budget 1993-present, Earth System Science Data, 10, 1551–1590, 2018.

Chen, J. L., Wilson, C. R., Tapley, B. D., Blankenship, D. D., and Ivins, E. R.: Patagonia icefield melting observed by gravity recovery and climate experiment (GRACE), Geophysical Research Letters, 34, 2007.

Cogley, J. G.: Geodetic and direct mass-balance measurements: comparison and joint analysis, Annals of Glaciology, 50, 96–100, 2009.

Crippen, R., Buckley, S., Agram, P., Belz, E., Gurrola, E., Hensley, S., Kobrick, M., Lavalle, M., Martin, J., Neumann, M., et al.: NASADEM Global Elevation Model: Methods And Progress, ISPRS - International Archives of the Photogrammetry, Remote Sensing and Spatial Information Sciences, XLI-B4, 125–128, https://doi.org/10.5194/isprs-archives-XLI-B4-125-2016, 2016.

Dall, J.: InSAR elevation bias caused by penetration into uniform volumes, IEEE Transactions on Geoscience and Remote Sensing, 45, 2319–2324, 2007.

Davies, B. J. and Glasser, N. F.: Accelerating shrinkage of Patagonian glaciers from the Little Ice Age (~AD 1870) to 2011, Journal of Glaciology, 58, 1063–1084, 2012.

Dee, D. P., Uppala, S. M., Simmons, A. J., Berrisford, P., Poli, P., Kobayashi, S., Andrae, U., Balmaseda, M. A., Balsamo, G., Bauer, P., et al.: The ERA-Interim reanalysis: configuration and performance of the data assimilation system, Quarterly Journal of the Royal Meteorological Society, 137, 553–597, https://doi.org/10.1002/qj.828, 2011.

Dietrich, R., Ivins, E., Casassa, G., Lange, H., Wendt, J., and Fritsche, M.: Rapid crustal uplift in Patagonia due to enhanced ice loss, Earth and Planetary Science Letters, 289, 22–29, 2010.

DLR-CAF: TanDEM-X Ground Segment - Raw DEM Specification (Project Internal), German Aerospace Center (DLR) - Cluster Applied Remote Sensing (CAF), CAF, DLR, Oberpfaffenhofen, Germany, 1.1 edn., doc. TD-PGS-TN-3081, 2010.

DLR-CAF: TerraSAR-X Ground Segment - Basic Product Specification Document, German Aerospace Center (DLR) - Cluster Applied Remote Sensing (CAF), CAF, DLR, Oberpfaffenhofen, Germany, 1.9 edn., doc. TX-GS-DD-3302, 2013.

DLR-EOC: TanDEM-X Ground Segment - DEM Products Specification Document, German Aerospace Center (DLR) - Earth Observation Center (EOC), EOC, DLR, Oberpfaffenhofen, Germany, 3.2 edn., https://tandemx-science.dlr.de/, doc. TD-GS-PS-0021, 2018.

Dowdeswell, J. and Vásquez, M.: Submarine landforms in the fjords of southern Chile: implications for glacimarine processes and sedimentation in a mild glacier-influenced environment, Quaternary Science Reviews, 64, 1–19, 2013.

Dussaillant, I., Berthier, E., and Brun, F.: Geodetic Mass Balance of the Northern Patagonian Icefield from 2000 to 2012 using two independent methods, Frontiers in Earth Science, 6, 8, 2018.

Farr, T. G., Rosen, P. A., Caro, E., Crippen, R., Duren, R., Hensley, S., Kobrick, M., Paller, M., Rodriguez, E., Roth, L., et al.: The Shuttle Radar Topography Mission, Reviews of Geophysics, 45, 2007.

Fernández, A. and Mark, B. G.: Modeling modern glacier response to climate changes along the Andes Cordillera: A multiscale review, Journal of Advances in Modeling Earth Systems, 8, 467–495, 2016.

Floricioiu, D. and Rott, H.: Seasonal and short-term variability of multifrequency, polarimetric radar backscatter of alpine terrain from SIR-C/X-SAR and AIRSAR data, IEEE Transactions on Geoscience and Remote Sensing, 39, 2634–2648, 2001.

Foresta, L., Gourmelen, N., Weissgerber, F., Nienow, P., Williams, J., Shepherd, A., Drinkwater, M., and Plummer, S.: Heterogeneous and rapid ice loss over the Patagonian Ice Fields revealed by CryoSat-2 swath radar altimetry, Remote Sensing of Environment, 211, 441–455, 2018.

Fritz, T., Rossi, C., Yague-Martinez, N., Rodriguez-Gonzalez, F., Lachaise, M., and Breit, H.: Interferometric processing of TanDEM-X data, in: 2011 IEEE International Geoscience and Remote Sensing Symposium (IGARSS), pp. 2428–2431, 2011.

Garreaud, R., Lopez, P., Minvielle, M., and Rojas, M.: Large-scale control on the Patagonian climate, Journal of Climate, 26, 215–230, 2013.

Glasser, N. F., Harrison, S., Jansson, K. N., Anderson, K., and Cowley, A.: Global sea-level contribution from the Patagonian Icefields since the Little Ice Age maximum, Nature Geoscience, 4, 303–307, 2011.

Hueso González, J., Bachmann, M., Krieger, G., and Fiedler, H.: Development of the TanDEM-X calibration concept: analysis of systematic errors, IEEE Transactions on Geoscience and Remote Sensing, 48, 716–726, 2010.

Ivins, E. R., Watkins, M. M., Yuan, D.-N., Dietrich, R., Casassa, G., and Rülke, A.: On-land ice loss and glacial isostatic adjustment at the Drake Passage: 2003-2009, Journal of Geophysical Research: Solid Earth, 116, https://doi.org/10.1029/2010JB007607, 2011.

Jacob, T., Wahr, J., Pfeffer, W. T., and Swenson, S.: Recent contributions of glaciers and ice caps to sea level rise, Nature, 482, 514–518, 2012.

Kalnay, E., Kanamitsu, M., Kistler, R., Collins, W., Deaven, D., Gandin, L., Iredell, M., Saha, S., White, G., Woollen, J., et al.: The NCEP/NCAR 40-year reanalysis project, Bulletin of the American Meteorological Society, 77, 437–471, 1996.

Krieger, G., Moreira, A., Fiedler, H., Hajnsek, I., Werner, M., Younis, M., and Zink, M.: TanDEM-X: A satellite formation for high-resolution SAR interferometry, IEEE Transactions on Geoscience and Remote Sensing, 45, 3317–3341, 2007.

Lachaise, M.: Phase Unwrapping of Multi-Channel Synthetic Aperture Radar Data: Application to the TanDEM-X Mission, Ph.D. thesis, Technische Universität München, http://elib.dlr.de/100297/, 2015.

Lachaise, M. and Fritz, T.: Phase unwrapping strategy and assessment for the high resolution DEMs of the TanDEM-X mission, in: 2016 IEEE International Geoscience and Remote Sensing Symposium (IGARSS), pp. 3223–3226, 2016.

Langhamer, L.: Lagrangian Detection of Moisture Sources for the Southern Patagonia Icefield, Master's thesis, Faculty for Geo- and Atmospheric Sciences, University of Innsbruck, Austria, 2017.

Langhamer, L., Sauter, T., and Mayr, G. J.: Lagrangian Detection of Moisture Sources for the Southern Patagonia Icefield (1979-2017), Frontiers in Earth Science, 6, 219, 2018.

Lee, J.-S., Hoppel, K. W., Mango, S. A., and Miller, A. R.: Intensity and phase statistics of multilook polarimetric and interferometric SAR imagery, IEEE Transactions on Geoscience and Remote Sensing, 32, 1017–1028, 1994.

Lopez, P., Chevallier, P., Favier, V., Pouyaud, B., Ordenes, F., and Oerlemans, J.: A regional view of fluctuations in glacier length in southern South America, Global and Planetary Change, 71, 85–108, 2010.

Malz, P., Meier, W., Casassa, G., Jaña, R., Skvarca, P., and Braun, M. H.: Elevation and mass changes of the Southern Patagonia Icefield derived from TanDEM-X and SRTM Data, Remote Sensing, 10, 188, 2018.

Marzeion, B., Champollion, N., Haeberli, W., Langley, K., Leclercq, P., and Paul, F.: Observation-Based Estimates of Global Glacier Mass Change and its Contribution to Sea-Level Change, Surveys in Geophysics, 38, 105–130, https://doi.org/10.1007/s10712-016-9394-y, 2017.

Mätzler, C.: Applications of the interaction of microwaves with the natural snow cover, Remote Sensing Reviews, 2, 259–387, 1987.

Minowa, M., Sugiyama, S., Sakakibara, D., and Skvarca, P.: Seasonal variations in ice-front position controlled by frontal ablation at Glaciar Perito Moreno, the Southern Patagonia Icefield, Frontiers in earth science, 5, 1, 2017.

Mouginot, J. and Rignot, E.: Ice motion of the Patagonian Icefields of South America: 1984–2014, Geophysical Research Letters, 42, 1441–1449, 2015.

Nagler, T. and Rott, H.: Retrieval of wet snow by means of multitemporal SAR data, IEEE Transactions on Geoscience and Remote Sensing, 38, 754–765, 2000.

NASA JPL: NASA Shuttle Radar Topography Mission Global 1 arc second [Data set]. NASA EOSDIS Land Processes DAAC., https://doi.org/10.5067/MEaSUREs/SRTM/SRTMGL1.003, 2013.

NASA JPL: NASA Shuttle Radar Topography Mission Swath Image Data [Data set]. NASA EOSDIS Land Processes DAAC., https://doi.org/10.5067/MEaSUREs/SRTM/SRTMIMGR.003, 2014.

NASA JPL: NASADEM Global Elevation Model (provisional), https://e4ftl01.cr.usgs.gov/provisional/MEaSUREs/NASADEM, accessed 31/1/2018, 2018.

Nuth, C. and Kääb, A.: Co-registration and bias corrections of satellite elevation data sets for quantifying glacier thickness change, The Cryosphere, 5, 271–290, 2011.

Paul, F., Barrand, N. E., Baumann, S., Berthier, E., Bolch, T., Casey, K., Frey, H., Joshi, S. P., Konovalov, V., Bris, R. L., et al.: On the accuracy of glacier outlines derived from remote-sensing data, Annals of Glaciology, 54, 171–182, 2013.

Pfeffer, W. T., Arendt, A. A., Bliss, A., Bolch, T., Cogley, J. G., Gardner, A. S., Hagen, J.-O., Hock, R., Kaser, G., Kienholz, C., et al.: The Randolph Glacier Inventory: a globally complete inventory of glaciers, Journal of Glaciology, 60, 537–552, 2014.

Rabus, B., Eineder, M., Roth, A., and Bamler, R.: The shuttle radar topography mission - a new class of digital elevation models acquired by spaceborne radar, ISPRS Journal of Photogrammetry and Remote Sensing, 57, 241–262, 2003.

Rasmussen, L. A., Conway, H., and Raymond, C. F.: Influence of upper air conditions on the Patagonia icefields, Global and Planetary Change, 59, 203–216, 2007.

Reber, B., Mätzler, C., and Schanda, E.: Microwave signatures of snow crusts modelling and measurements, International Journal of Remote Sensing, 8, 1649–1665, 1987.

RGI Consortium: Randolph Glacier Inventory–A Dataset of Global Glacier Outlines: Version 6.0: Technical Report, Global Land Ice Measurements from Space, Colorado, USA, Digital Media. https://doi.org/10.7265, 2017.

Rignot, E., Rivera, A., and Casassa, G.: Contribution of the Patagonia Icefields of South America to sea level rise, Science, 302, 434–437, 2003.

Rivera, A.: Mass balance investigations at Glaciar Chico, Southern Patagonia Icefield, Chile, Ph.D. thesis, University of Bristol, 2004.

Rivera, A., Benham, T., Casassa, G., Bamber, J., and Dowdeswell, J. A.: Ice elevation and areal changes of glaciers from the Northern Patagonia Icefield, Chile, Global and Planetary Change, 59, 126–137, 2007.

Rivera, A., Koppes, M., Bravo, C., and Aravena, J. C.: Little ice age advance and retreat of Glaciar Jorge Montt, Chilean Patagonia, Climate of the Past, 8, 403–414, 2012.

Rizzoli, P., Martone, M., Gonzalez, C., Wecklich, C., Tridon, D. B., Bräutigam, B., Bachmann, M., Schulze, D., Fritz, T., Huber, M., et al.: Generation and performance assessment of the global TanDEM-X digital elevation model, ISPRS Journal of Photogrammetry and Remote Sensing, 132, 119–139, 2017.

Rodriguez, E., Morris, C. S., Belz, J. E., Chapin, E. C., Martin, J. M., Daffer, W., and Hensley, S.: An assessment of the SRTM topographic products, Tech. Rep. D-31639, Jet Propulsion Laboratory, 2005.

Rolstad, C., Haug, T., and Denby, B.: Spatially integrated geodetic glacier mass balance and its uncertainty based on geostatistical analysis: application to the western Svartisen ice cap, Norway, Journal of Glaciology, 55, 666–680, 2009.

Rossi, C., Eineder, M., Fritz, T., and Breit, H.: TanDEM-X Mission: Raw DEM Generation, in: EUSAR 2010; 8th European Conference on Synthetic Aperture Radar, pp. 1–4, 2010.

Rossi, C., Rodriguez-Gonzalez, F., Fritz, T., Yague-Martinez, N., and Eineder, M.: TanDEM-X calibrated Raw DEM generation, ISPRS Journal of Photogrammetry and Remote Sensing, 73, 12–20, 2012.

Rott, H., Abdel Jaber, W., Wuite, J., Scheiblauer, S., Floricioiu, D., van Wessem, J. M., Nagler, T., Miranda, N., and van den Broeke, M. R.: Changing pattern of ice flow and mass balance for glaciers discharging into the Larsen A and B embayments, Antarctic Peninsula, 2011 to 2016, The Cryosphere, 12, 1273–1291, https://doi.org/10.5194/tc-12-1273-2018, 2018.

Schaefer, M., Machguth, H., Falvey, M., and Casassa, G.: Modeling past and future surface mass balance of the Northern Patagonia Icefield, Journal of Geophysical Research: Earth Surface, 118, 571–588, 2013.

Seal, D. and Rogez, F.: SRTM As-Flown Mission Timeline, Tech. rep., JPL NASA, http://www2.jpl.nasa.gov/srtm/SRTM_TIM_AF.pdf, 2000.

Stuefer, M., Rott, H., and Skvarca, P.: Glaciar Perito Moreno, Patagonia: climate sensitivities and glacier characteristics preceding the 2003/04 and 2005/06 damming events, Journal of Glaciology, 53, 3–16, 2007.

Tiuri, M. E., Sihvola, A. H., Nyfors, E. G., and Hallikaiken, M. T.: The complex dielectric constant of snow at microwave frequencies, IEEE Journal of Oceanic Engineering, 9, 377–382, 1984.

Ulaby, F. T., Long, D. G., Blackwell, W. J., Elachi, C., Fung, A. K., Ruf, C., Sarabandi, K., Zebker, H. A., and Van Zyl, J.: Microwave radar and radiometric remote sensing, vol. 4, University of Michigan Press Ann Arbor, 2014.

Warren, C. and Aniya, M.: The calving glaciers of southern South America, Global and Planetary Change, 22, 59–77, 1999.

Weidemann, S. S., Sauter, T., Malz, P., Jaña, R. A., Arigony-Neto, J., Casassa, G., and Schneider, C.: Glacier mass changes of lake-terminating Grey and Tyndall glaciers at the Southern Patagonia Icefield derived from geodetic observations and energy and mass balance modeling, Frontiers in Earth Science, 6, 81, 2018.

Wendleder, A., Felbier, A., Wessel, B., Huber, M., and Roth, A.: A Method to Estimate Long-Wave Height Errors of SRTM C-Band DEM, IEEE Geoscience and Remote Sensing Letters, 13, 696–700, https://doi.org/10.1109/LGRS.2016.2538822, 2016.

Wessel, B., Huber, M., Wohlfart, C., Marschalk, U., Kosmann, D., and Roth, A.: Accuracy assessment of the global TanDEM-X Digital Elevation Model with GPS data, ISPRS Journal of Photogrammetry and Remote Sensing, 139, 171–182, 2018.

Willis, M. J., Melkonian, A. K., Pritchard, M. E., and Ramage, J. M.: Ice loss rates at the Northern Patagonian Icefield derived using a decade of satellite remote sensing, Remote Sensing of Environment, 117, 184–198, 2012a.

Willis, M. J., Melkonian, A. K., Pritchard, M. E., and Rivera, A.: Ice loss from the Southern Patagonian Ice Field, South America, between 2000 and 2012, Geophysical Research Letters, 39, 2012b.

Wilson, R., Carrión, D., and Rivera, A.: Detailed dynamic, geometric and supraglacial moraine data for Glaciar Pio XI, the only surge-type glacier of the Southern Patagonia Icefield, Annals of Glaciology, 57, 119–130, 2016.

Wuite, J., Rott, H., Hetzenecker, M., Floricioiu, D., de Rydt, J., Gudmundsson, H., Nagler, T., and Kern, M.: Evolution of surface velocities and ice discharge of Larsen B outlet glaciers from 1995 to 2013, The Cryosphere, 9, 957–969, 2015.